

# The COS-legacy survey of C IV absorbers: properties and origins of the intervening systems

Aditya Manuwal,<sup>1,2\*</sup> Anand Narayanan,<sup>2</sup> Purvi Udhvani,<sup>2</sup> Raghunathan Srianand,<sup>3</sup> Blair D. Savage,<sup>4</sup> Jane C. Charlton<sup>5</sup> and Toru Misawa<sup>6</sup>

<sup>1</sup>International Centre for Radio Astronomy Research, University of Western Australia, 35 Stirling Highway, Crawley, WA 6009, Australia

<sup>2</sup>Department of Earth and Space Sciences, Indian Institute of Space Science & Technology, Thiruvananthapuram 695547, Kerala, India

<sup>3</sup>Inter-University Centre for Astronomy and Astrophysics, Post Bag 4, Pune 411007, India

<sup>4</sup>Department of Astronomy, The University of Wisconsin-Madison, 5534 Sterling Hall, 475 N. Charter Street, Madison, WI 53706-1582, USA

<sup>5</sup>The Pennsylvania State University, 413 Davey Lab, University Park, State College, PA 16802, USA

<sup>6</sup>School of General Education, Shinshu University, 3-1-1 Asahi, Matsumoto, Nagano 390-8621, Japan

Accepted 2021 May 26. Received 2021 May 26; in original form 2020 September 8

## ABSTRACT

We present here results from a survey of intervening C IV absorbers at  $z < 0.16$  conducted using 223 sightlines from the Hubble Spectroscopic Legacy Archive. Most systems (83%) out of the total sample of 69 have simple kinematics with 1 or 2 C IV components. In the 22 C IV systems with well constrained HI column densities, the temperatures from the  $b$ -values imply predominantly photoionized plasma ( $T \leq 10^5$  K) and non-thermal dynamics. These systems also have solar or higher metallicities. We obtain a C IV line density of  $dN/dX = 5.1 \pm 1.0$  for  $\log[N(\text{C IV}) (\text{cm}^{-2})] \geq 12.9$ , and  $\Omega_{\text{C IV}} = (8.01 \pm 1.62) \times 10^{-8}$  for  $12.9 \leq \log[N(\text{C IV}) (\text{cm}^{-2})] \leq 15.0$ . The C IV bearing diffuse gas in the  $z < 0.16$  Universe has a metallicity of  $(2.07 \pm 0.43) \times 10^{-3} Z_{\odot}$ , an order of magnitude more than the metal abundances in the IGM at high redshifts ( $z \gtrsim 5$ ), and consistent with the slow build-up of metals in the diffuse circum/intergalactic space with cosmic time. For  $z < 0.015$  (complete above  $L > 0.01L^*$ ), the Sloan Digital Sky Survey provides a tentative evidence of declining covering fraction for strong C IV ( $N > 10^{13.5} \text{ cm}^{-2}$ ) with  $\rho$  (impact parameter) and  $\rho/R_{\text{vir}}$ . However, the increase at high separations suggests that strong systems are not necessarily coincident with such galaxies. We also find that strong C IV absorption at  $z < 0.051$  is not coincident with galaxy over-dense regions complete for  $L > 0.13L^*$ .

**Key words:** quasars: absorption lines – galaxies: clusters: general – intergalactic medium – techniques: spectroscopic – methods: data analysis

## 1 INTRODUCTION

In the past few decades, results from simulations of galaxy formation in the frame-work of large cosmological volumes (Cen & Ostriker 1999; Davé et al. 1999; Dave et al. 2001) and observations (Fukugita et al. 1998; Fukugita & Peebles 2004; Shull et al. 2012; Stocke et al. 2013; Werk et al. 2014; Prochaska et al. 2017) have established that most of the baryons reside outside the stellar disks of galaxies in the circumgalactic (CGM) or intergalactic medium (IGM). The gaseous clouds containing these baryons exist in a multi-phase structure and have substantial influence on the evolution of galaxies. The IGM contributes baryons to the galaxies through gravitational infall of gas clouds. Galaxies in turn enrich the CGM and the IGM through metal rich outflows initiated by supernova/starburst driven galactic scale winds, or tidal interactions (Heckman et al. 1990, 2001; Martin et al. 2002; Scannapieco et al. 2002; Hopkins et al. 2006; Keeney et al. 2006; Songaila 2006; Rupke & Veilleux 2011; Tripp et al. 2011; Tumlinson et al. 2011; Stocke et al. 2013; Muzahid et al. 2015; Keeney et al. 2017; Pratt et al. 2018).

Even at low redshifts ( $z \lesssim 0.5$ ), the mass fraction of baryons in the cool ( $T \sim 10^4$  K), warm ( $T \sim 10^5 - 10^6$  K) and in the hot ( $T > 10^6$  K) phase outside of the star forming regions of galaxies far outweighs the mass fraction inside galaxies (Salucci & Persic 1999; Dave et al. 2001; Fukugita & Peebles 2004). An observational census of the baryons in the low redshift Universe is incomplete without properly accounting for the warm-hot phase. Since the gas at  $T < 10^6$  K can be detected using absorption lines in spectra of background sources at high redshift (like GRBs or QSOs), a plethora of absorption line studies have been focused on detecting these baryonic reservoirs in the circumgalactic and intergalactic space around galaxies, characterizing their physical properties and chemical abundances, and understanding their origins (e.g. Fang et al. 2010; Danforth et al. 2011; Narayanan et al. 2011; Burchett et al. 2018, and references therein).

The cool phase also possesses a significant fraction of baryonic matter in the local Universe ( $\sim 30\%$ ) (Penton et al. 2004; Lehner et al. 2007) and has therefore been explored extensively through Mg II (e.g. Narayanan et al. 2005; Chen et al. 2010; Churchill et al. 2013; Nielsen et al. 2015; Bowen et al. 2016), C IV (e.g. Schaye et al. 2003; Songaila 2006; Schaye et al. 2007; Cooksey et al. 2010; Burchett

\* E-mail: aditya.manuwal@icrar.org

et al. 2013), and also C II and Si II which are used as proxies for Mg II. C IV traces a higher ionization, more diffuse phase than Mg II with densities that are lower by 1 - 2 orders of magnitude (Ding et al. 2003; Charlton et al. 2003). Multiple, but closely separated, lines of sight observations show this phase to be more smoothly distributed over sub-kiloparsec to several kiloparsec scales; potentially tracing the diffuse photoionized halos of galaxies (Lopez et al. 1999; Rauch et al. 2001). Based on these, Mg II seems to be tracing compact pockets of high density gas, often having high metallicity (near-solar or solar), and with sizes of a few tens of parsec, whereas C IV covers a larger dynamic range.

It has been shown that cool gas clouds can serve as tools to comprehend chemical enrichment, physical conditions and the effect of environment on the CGM (Stocke et al. 2013; Yoon & Putman 2013; Burchett et al. 2016; Keeney et al. 2017; Lehner et al. 2018). In galaxy dense environments like rich groups and clusters, most of the gas is shock heated to temperatures of  $T > 10^7$  K (Mushotzky et al. 1978; Loken et al. 2002; Roncarelli et al. 2006; De Grandi et al. 2004) and cool gas clouds can arise in intergalactic/intracluster space through thermal instability (Maller & Bullock 2004; Thompson et al. 2016), or stripping mechanisms like galaxy mergers (Hani et al. 2017; Burchett et al. 2018), tidal interactions (Morris & Bergh 1993) and ram pressure (Abadi et al. 1999). This implies that the chemical and physical properties of cool gas clouds, along with their large scale environment, can be used to gain insights about their origins, and the physical mechanisms involved in interactions of the galaxies with their surrounding medium which play key roles in galaxy evolution. It is better to carry out such studies at low redshifts since that allows exploring relationships between absorbers and nearby galaxies, especially sub- $L^*$  galaxies which contribute significantly to feedback processes.

C IV or triply ionized carbon is an excellent tracer of enriched, diffuse cool gas (Buson & Ulrich 1990; Jenkins et al. 2003; Schaye et al. 2003; Simcoe et al. 2004; Songaila 2006; Fox et al. 2007; Schaye et al. 2007; Tejos et al. 2009; Ranquist & Kim 2012; Burchett et al. 2013, 2016; Burchett et al. 2018). Most of the earlier studies were focused on absorbers at high redshifts ( $z \gtrsim 1.5$ ). Rauch (1998) used simulations of the  $z \sim 3$  universe and predicted that C IV is a good tracer of filaments and small protogalactic clouds. Surveys of C IV absorbers at high redshifts claim the gas to be mostly photoionized with median  $[C/H] \sim -3$  (Schaye et al. 2003; Simcoe et al. 2004), and dominated by thermal energy (Ranquist & Kim 2012). Songaila (2006) finds most low column density absorbers to reside in the IGM and suggests that half of the high column density systems are possibly produced by outflows. The metal rich systems at these redshifts are compact and short lived, which also suggests transport of metals into the IGM (Schaye et al. 2007).

The advent of the Cosmic Origins Spectrograph (COS) onboard the Hubble Space Telescope (*HST*) has offered a unique opportunity for conducting such surveys at low redshift owing to its unprecedented sensitivity and performance. The studies that followed show that C IV absorbers at low redshifts can represent both collisional and photoionized gas (Danforth & Shull 2008), and the ones within galactic halos tend to be metal rich (Stocke et al. 2013). As expected, they are also associated with star forming galaxies and strong outflows are required to explain the observations (Bordoloi et al. 2014). Such clouds are also seen to be accreted by galaxies (Burchett et al. 2013). The largest blind survey of C IV absorbers yet at  $z < 0.16$  was done using the *HST*/COS spectra towards 89 QSO sightlines (Burchett et al. 2015, 2016) but their results based on ion-ion relations are not statistically significant since the survey was limited to

a small sample size and a study with a larger sample is required; as also emphasized by Burchett et al. (2015).

In this study, we use the data from the Hubble Spectroscopic Legacy Archive<sup>1</sup> (Peebles et al. 2017) to identify C IV absorbers at  $z < 0.16$  in the FUV spectra of 223 background quasars. Through this work we aim to leverage better statistics provided by the archive and thus conduct the largest survey of such absorption systems at low redshift. We infer the physical conditions and chemical enrichment of the clouds by drawing interpretations from ionization modelling and considering their galaxy environments and use these as contexts to hypothesize on the origins of C IV absorbers. This paper is divided into 7 sections. Sec. 2 delineates the methodology behind selecting the systems in our sample. The completeness of this survey is limited by the achieved spectral signal-to-noise ratio, this has been addressed in Sec. 3. The techniques involved in measuring absorption line properties and results from those measurements are described in Sec. 4. The absorber statistics and related parameters are derived in Sec. 5. In Sec. 6, we describe the ionization modelling of absorbers and the cloud properties derived from it. Sec. 7 explores the distribution and properties of galaxies around the absorbers. We summarize the results in Sec. 8. Additionally, we hypothesize about the plausible origins of some specific clouds in a document provided as supplementary material, and we recommend the reader to go through it as well. Throughout the paper, we adopt the cosmology with  $H_0 = 69.6 \text{ km s}^{-1} \text{ Mpc}^{-1}$ ,  $\Omega_m = 0.286$  and  $\Omega_\Lambda = 0.714$  from Bennett et al. (2014). All the logarithmic values mentioned are in base-10. The python routines used for data analysis in this study can be found at our online repository<sup>2</sup>.

## 2 SYSTEM SELECTION

For generating a statistically significant sample of C IV absorbers, we have used *HST*/COS FUV archival spectra of 223 quasars. The spectroscopic abilities of COS and its in-flight performances are given in Green et al. (2012) and Osterman et al. (2011). The FUV wavelength coverage of the data lies in the range of 1136 – 1795 Å at medium spectral resolutions (FWHM) of  $\sim (17 - 20) \text{ km s}^{-1}$ . The data acquisition involved both G130M and G160M gratings for 216 sightlines, and only G160M grating for the other 7 sightlines. This limits the C IV survey redshift to  $z_{\text{max}} \sim 0.157$  requiring coverage of both members of the C IV doublet. Continuum models were generated for each spectrum by fitting low order polynomials locally to  $\sim 10 - 20 \text{ Å}$  wavelength blocks, excluding regions with absorption features, and covering broad emission lines.

The search for C IV lines was carried out with the following conditions: (1) the spectrum should cover both  $\lambda 1548$  and  $\lambda 1550$  transitions of the doublet with visually similar profiles, (2) the C IV  $\lambda 1548$  line should have a formal detection significance of  $\geq 3\sigma$ , (3) the equivalent width ratio for the unsaturated C IV  $\lambda 1548, 1550$  lines that are not blended with some other absorption should be approximately consistent with their expected value of  $\approx 2 : 1$  within the measurement uncertainty, and (4) the absorber should be at  $|\Delta v| > 5000 \text{ km s}^{-1}$  from the emission redshift of the background quasar, for it to be not associated with the quasar (Foltz et al. 1986; Misawa et al. 2007; Ganguly et al. 2013; Muzahid et al. 2013). The profiles were checked for contaminations by comparing the apparent column density profiles of the doublet transitions, and using the line identifications<sup>3</sup>

<sup>1</sup> [https://archive.stsci.edu/hst/spectral\\_legacy/](https://archive.stsci.edu/hst/spectral_legacy/)

<sup>2</sup> <https://github.com/adimanuwal/ROQALS>

<sup>3</sup> <https://archive.stsci.edu/prepds/igm/>

provided by Danforth et al. (2016). An absorber is included in our sample only if all of the above criteria are satisfied. A search was carried out through each sightline by blindly assuming every absorption feature redward of 1548 Å to be a CIV  $\lambda 1548$  line. The corresponding 1550 Å line was then searched for at its redshifted wavelength. For every positive matching of the doublets, the apparent column density profiles were also inspected for agreement. As additional validation, the presence of other metal lines and H I at this redshift were also considered, though this was not a necessary condition for claiming a CIV detection. The pixel in the CIV  $\lambda 1548$  feature with the maximum optical depth was used to define the redshift of the system. For saturated CIV components, we adopt the redshift corresponding to the saturated pixel with the lowest velocity.

### 3 SURVEY COMPLETENESS

The 223 archival QSO spectra were obtained as part of different observing programs and hence have varying levels of spectral sensitivity towards the detection of lines. The sample constitutes spectroscopic data that was available through the Hubble Spectroscopic Legacy Archive as of June 2017. From this larger sample, we excluded 10 sightlines that did not offer any path length for CIV systems based on our search criteria explained later. To assess the completeness of our survey and to better understand the statistical implications of our results, cumulative redshift path lengths for CIV over the column density range of  $N(\text{CIV}) = 10^{12.8} - 10^{14.9} \text{ cm}^{-2}$  are determined (which encompasses the *total* CIV column density in our systems<sup>4</sup>). The path length along a given sightline is estimated by summing  $\Delta z$  over only those pixels where a CIV detection is possible, avoiding wavelengths where search is impossible due to the presence of Galactic or spectral features intrinsic to the QSO, gaps in the data, and a few narrow regions with sharp variations in the quasar continuum due to noise. Some of the sightlines were observed to probe IGM/CGM around known galaxies. Since this is a blind survey, we also exclude the spectral regions within  $|\Delta v| < 500 \text{ km s}^{-1}$  of the targeted galaxies in such sightlines when computing pathlengths or absorber statistics. We use the formalism given in Burchett et al. (2015) for calculating the rest-frame equivalent width threshold required for a  $3\sigma$  detection of the CIV  $\lambda 1548$  line with a column density of  $N(\text{CIV})$ . The rest equivalent width limit  $W_{\text{lim}}$  for a  $N_\sigma$  detection of the feature centered at a pixel located at the wavelength corresponding to redshift  $z$  is

$$W_{\text{lim}} = \frac{N_\sigma \sigma_w}{1+z}, \quad (1)$$

where  $N_\sigma = 3$  is the desired detection significance, and  $\sigma_w$  is the uncertainty in equivalent width calculated over a  $102 \text{ km s}^{-1}$  wide region, which is the mean width of *total* CIV absorption in our systems. It is determined as

$$\sigma_w = \sqrt{\sum_i \left( \frac{\sigma_{I_i} \Delta \lambda_i}{I_i} \right)^2}, \quad (2)$$

where  $I_i$  is the continuum flux at the  $i$ th pixel,  $\sigma_{I_i}$  is the uncertainty in  $I_i$ , and  $\Delta \lambda_i$  is wavelength interval at the pixel. The  $W_{\text{lim}}$  value is converted to corresponding column density threshold  $N_{\text{lim}}$  assuming the line to be on the Curve of Growth (CoG) for  $b(\text{CIV}) = 14 \text{ km s}^{-1}$ ; the mean  $b$ -value for our sample (the CoG is generated using the

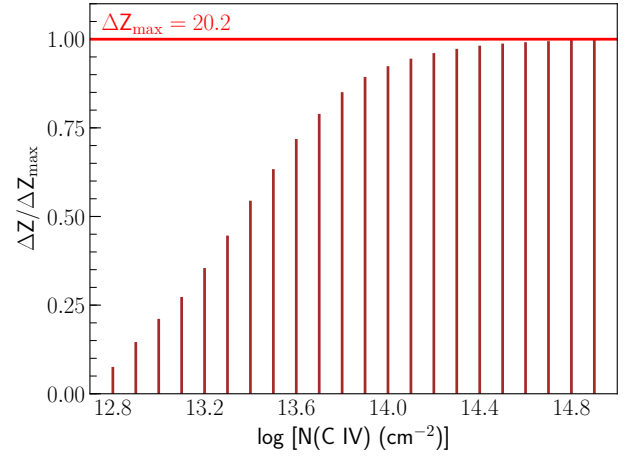


**Figure 1.** The cumulative redshift path length for different CIV column densities of  $\lambda 1548$  normalized by  $\Delta Z_{\text{max}} = 20.2$ , which corresponds to  $\Delta Z$  for  $N(\text{CIV}) = 10^{14.9} \text{ cm}^{-2}$ .

VOIGTFIT python module<sup>5</sup>. Along a given sightline, we only examine pixels at  $z > 0.00167$  considering that the line should arise from an extragalactic cloud displaced by  $|\Delta v| > 500 \text{ km s}^{-1}$  from  $z = 0$  (McClure-Griffiths et al. 2009). This corresponds to an observed wavelength of  $\sim 1550.78 \text{ Å}$  for  $\lambda 1548$  which is well within the FUV coverage of COS. We should mention here that all the 223 QSOs have  $z_{\text{em}} > 0.01852$ , or  $\Delta v > 500 \text{ km s}^{-1}$  with respect to  $z = 0.00167$ . The maximum redshift for consideration depends on two factors: (1) non-association with the QSO ( $|\Delta v| > 5000 \text{ km s}^{-1}$  from the quasar redshift) and, (2) coverage of the  $\lambda 1550$  line of the doublet.

A line with a given  $N(\text{CIV})$  will be a  $3\sigma$  detection only at those pixels where  $N_{\text{lim}} < N(\text{CIV})$ . For a  $k$ -th sightline, the total path-length  $\Delta z_k$  for  $N(\text{CIV})$  is the sum of all such pixels. The cumulative redshift path length  $\Delta Z$  for this  $N(\text{CIV})$  is determined by coadding such redshift path lengths for the entire sample of 223 QSOs in the following manner,

$$\Delta Z = \sum_{k=1}^M \Delta z_k, \quad (3)$$

where  $M = 223$  is the number of sightlines. The resultant pathlengths are tabulated in Table 1. The cumulative redshift path lengths for a  $3\sigma$  CIV detection suggest that the survey reaches  $\Delta Z_{\text{max}} = 20.2$  for  $N(\text{CIV}) = 10^{14.9} \text{ cm}^{-2}$ . This is almost a two fold increase compared to earlier such surveys by Burchett et al. (2015) and Danforth et al. (2016), which had  $\Delta Z = 12.9$  and  $\Delta Z = 8.85$ , respectively.

We discovered 69 CIV absorbers spanning the redshift interval  $0.002 < z < 0.154$  that satisfied the selection criteria mentioned in Sec. 2. This sample is larger by 27 compared to Burchett et al. (2015), and by 1 compared to Danforth et al. (2016), which searched for systems in the same redshift range. The basic properties of all absorbers are summarized in Table 2 and Table 3. Our sample has an overlap of 3 systems with Cooksey et al. (2010), 18 systems with that of Burchett et al. (2015), and 26 with Danforth et al. (2016). The reader may refer to Table 2 for individual cases.

<sup>4</sup> The  $z_{\text{abs}} = 0.08940$  system towards QSO B1435-0645 has a saturated CIV component that is excluded from analysis in this paper

<sup>5</sup> <https://github.com/jkrogager/VoigtFit>

**Table 1.** Pathlengths for different C IV column densities

$\log [N(\text{C IV}) (\text{cm}^{-2})]$ (1)	$W_r(\lambda 1548) (\text{m}\text{\AA})$ (2)	$\Delta Z$ (3)	$\Delta X$ (4)	$N$ (5)
12.8	23.7	1.6	1.8	0
12.9	29.3	3.0	3.3	2
13.0	36.0	4.4	4.8	0
13.1	44.1	5.6	6.2	3
13.2	53.5	7.3	8.1	1
13.3	64.5	9.2	10.1	1
13.4	77.0	11.2	12.4	3
13.5	91.0	12.9	14.3	3
13.6	105.7	14.7	16.2	3
13.7	121.4	16.1	17.8	6
13.8	137.2	17.3	19.2	4
13.9	152.8	18.1	20.1	4
14.0	167.5	18.7	20.8	2
14.1	181.1	19.1	21.3	4
14.2	193.7	19.4	21.6	8
14.3	205.1	19.7	21.9	5
14.4	215.7	19.8	22.1	2
14.5	225.7	19.9	22.2	1
14.6	235.1	20.0	22.3	0
14.7	244.2	20.1	22.3	0
14.8	252.8	20.1	22.4	0
14.9	261.2	20.2	22.5	0

(1) C IV column density; (2) Equivalent width correspond to the column density according to  $\lambda 1548$  CoG for  $b(\text{C IV}) = 14 \text{ km s}^{-1}$ ; (3) Redshift pathlength for  $\geq 3\sigma$  detection based on the formalism of Eq. 1 and Eq. 3; (4) Co-moving pathlength; (5) Number of absorbers within  $\pm 0.05$  dex of the logarithmic column density (excluding the systems around targeted galaxies).

#### 4 ABSORBER LINE MEASUREMENTS

The line measurements are carried out using two methods: (1) the integrated apparent optical depth (AOD) method given by [Savage & Sembach \(1991\)](#) and (2) Voigt profile fitting using the VPFIT routine (version 12.1; [Carswell & Webb 2014](#)), where the profiles are convolved with the relevant model COS instrumental spread functions<sup>6</sup>. We have accounted for COS lifetime positions while selecting the line spread functions. In addition to constraining the column density, the best-fit models also provide the centroids of the absorption features and the line widths in terms of the Doppler parameter  $b$  in  $\text{km s}^{-1}$ . Wavelength calibration of COS is known to possess residual offsets as large as  $|\Delta\nu| = 40 \text{ km s}^{-1}$  (see appendix of [Wakker et al. 2015](#)). Velocity offsets of  $\leq 40 \text{ km s}^{-1}$  between lines in an individual absorber are therefore treated as within this systematic uncertainty.

Profiles are simultaneously fitted to all available absorption lines from the same ion. For two ions that are known to trace gas of similar ionization (e.g., C II and Si II, or C IV and Si IV), the model fits to the lines were guided fits (in terms of the number of components, and their velocity centroids), if adequate constraints are otherwise not available. Only those lines that are detected at  $3\sigma$ , with no obvious indication of contamination<sup>7</sup>, are included in the fitting. VPFIT compensates for mild levels of line saturation, especially while fitting multiple lines from the same ion. C IV  $\lambda 1550$  is a weaker line

<sup>6</sup> <https://www.stsci.edu/hst/instrumentation/cos/performance/spectral-resolution>

<sup>7</sup> Based on the comparison of apparent column density profiles of multiple transitions from the same ion, and features identified by [Danforth et al. \(2016\)](#)

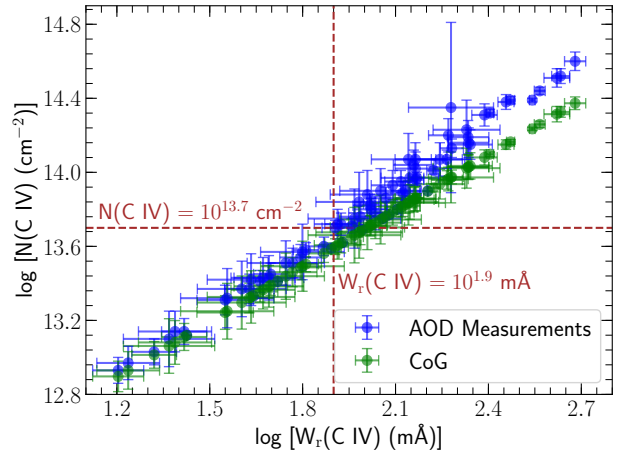


**Figure 2.** Comparison of C IV  $\lambda 1550$  column densities measured using the AOD method with those predicted by the linear part of CoG for the measured rest-frame equivalent widths. The comparison shows that line saturation begins for  $N(\text{C IV}) \gtrsim 10^{13.7} \text{ cm}^{-2}$ .

than C IV  $\lambda 1548$  and therefore an accurate estimation of C IV column density is governed by the saturation level of  $\lambda 1550$ . It is possible to have a constrained measurement for C IV in a system with a saturated  $\lambda 1548$  if the  $\lambda 1550$  is moderate to mildly saturated, because both lines of the doublet are fit together with Voigt profile models, which provides a unique solution of  $b$  and  $N$ . We assess the saturation level of our profiles through a combination of visual inspection and comparison with the linear part of CoG (Fig. 2). We consider a line to be saturated if the measured column density and that based on the linear CoG are not consistent within their uncertainties. The lowest column density where this happens is  $N(\text{C IV}) = 10^{13.7} \text{ cm}^{-2}$ . This line has  $W_r = 79.43 \text{ m}\text{\AA}$  which implies a  $b(\text{C IV}) \approx 15$ , close to the median  $b(\text{C IV})$  in our sample.

In addition to the Doppler  $b$  parameter, the overall kinematics of the C IV profiles are estimated through  $\Delta v_{90}$  ([Prochaska & Wolfe 1997](#)). The  $\Delta v_{90}$  width is calculated as the velocity range of the absorption profile containing 90% of the integrated apparent optical depth. In other words, this value corresponds to the velocity difference between the two pixels across the full range of absorption whose cumulative optical depths are 5% and 95% of the total.

#### 4.1 Column density of saturated H I

The COS spectra mainly cover only Ly $\alpha$  amongst the H I lines for the redshift range of C IV absorbers in this survey. In most cases, the Ly $\alpha$  components are significantly saturated. In the 69 absorbers featured in this paper, Ly $\beta$  is covered only in 11, which are near to the redshift upper limit of the sample of  $z \approx 0.16$ . In cases where the Ly $\beta$  is unsaturated, accurate estimations of  $N(\text{H I})$  are possible. In an additional 11 absorbers, components of Ly $\alpha$  itself are unsaturated or mildly saturated. Voigt profile fits predict a narrow range of  $N(\text{H I})$  for these as well. Thus, altogether there are 22 absorbers for which well-constrained H I measurements are possible. We refer to these as the ‘‘sample with secure H I’’. For the rest, the profile models do not yield a unique solution for the  $N$ ,  $b$  and  $v$  of the absorbing component(s) due to line saturation. But, however large, there can only be a finite number of combinations of  $N$  and  $b$  that can reproduce a given saturated profile, especially at the profile edges. Moreover, if the C IV (or any other metal line) is devoid of saturation and spans the same velocity as the saturated H I, it is likely that the C IV and

the H I represent the same cloud. In such cases, we also adopt for H I the same component structure as C IV, with the caveat that H I can be more widely distributed and kinematically more complex than the metal lines. We implement these ideas to constrain the  $b(\text{H I})$  and the  $N(\text{H I})$  for such saturated Ly $\alpha$  components as explained below.

We begin by adopting the well constrained Doppler  $b$  parameter for C IV based on a simultaneous free profile fit to the doublet lines. The lower and upper limits on  $b(\text{H I})$  are then found by assuming the two extremes in line broadening; the entirely non-thermal [ $b(\text{H I}) = b(\text{C IV})$ ] scenario, and the fully thermal [ $b(\text{H I}) = 3.452 \times b(\text{C IV})$ ] scenario. This is done for aligned H I and C IV components, in cases where the H I component structure is evident. For strongly saturated H I lines, the component structure is assumed to be the same as C IV. The limiting  $b$ -values for H I thus obtained are used to generate model Voigt profiles using VPFIT for the saturated H I. A plausible range for the H I column density is finally inferred by accepting those  $N$  and  $b$  combinations that yield fits consistent with the observed H I. The column density and  $b$ -parameter thus inferred carry a wide uncertainty range for  $N$  and  $b$  compared to the sample with secure H I. It should be noted that the  $N(\text{H I})$  range thus derived represents the broadest possible range for H I in the cloud that has the C IV. The actual range might be narrower, as some H I might not be associated with C IV but rather correspond to a phase with different ionization conditions compared to the phase where the C IV originates.

#### 4.2 Absorption properties and their correlations

As shown in Table 3, 75% of the systems have elements that are heavier than carbon, possibly indicating that C IV absorbers trace highly enriched gas. A majority of the systems (57/69, 83%) have a kinematically simple C IV profile with only one or two absorbing components. Complex absorption profiles with a large number of components in either H I or C IV are rare in this sample. However, there can be very narrow components that went undetected due to the limited resolution of COS. The entire sample is comprised of 127 (including the saturated C IV component) and 168 kinematically distinct components in C IV and H I, respectively. Savage et al. (2014) carried out an unbiased survey of O VI absorbers and showed that 90% of the systems have two or fewer O VI components. Thus, the most common C IV and O VI absorptions tracing CGM and IGM occur in kinematically simple systems at the resolution of COS.

In Fig. 3, we compare the H I and C IV column densities in each component. We find no clear correlation between the two column densities, suggesting that the population of C IV absorbers are possibly tracing a range of physical conditions, if the C IV and H I are from the same gas phase. This can also be deduced by comparing the range of column densities for C IV and H I (see Table 3). The C IV column densities for the sample spans two orders of magnitude whereas the corresponding H I values are spread over four orders of magnitude. This lack of correlation is perhaps an indication of metals being confined to patchy zones in a wide range of H I environments. It is interesting to note that there are a few absorbers where the  $N(\text{C IV}) \gtrsim N(\text{H I})$ , indicated by the points near to and below the dashed line in Fig. 3. Such systems where the C IV column density is comparable to or greater than H I are likely to be extremely metal-rich gas clouds in the circumgalactic and intergalactic space similar to the population of C IV absorbers discussed in Schaye et al. (2007).

The  $z_{\text{abs}} = 0.13850$  system towards PG 1116+215 shows Ly $\alpha$  and Ly $\beta$  absorption but both are saturated. We therefore adopt the  $b(\text{H I})$  and  $N(\text{H I})$  from Sembach et al. (2004) who used higher order Lyman series lines from HST/STIS to constrain the H I column

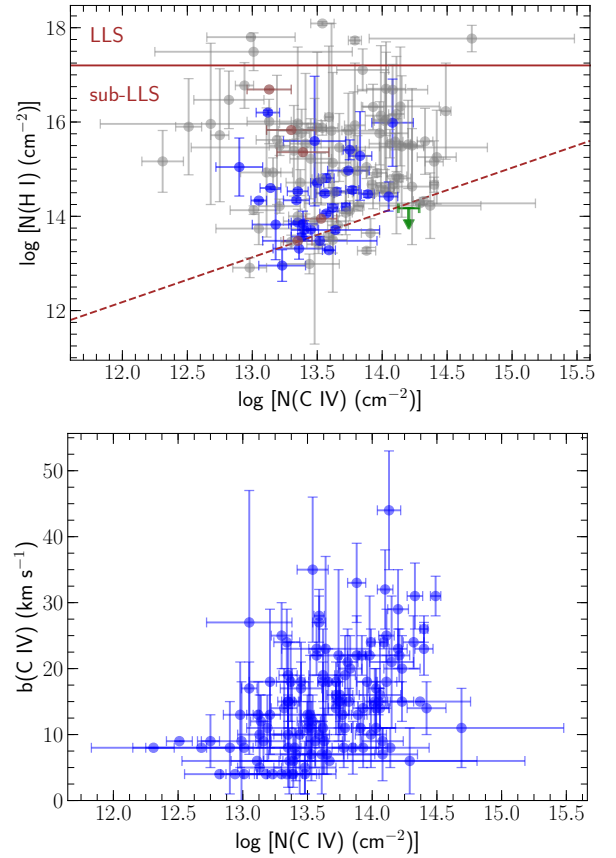


**Figure 3.** Top: The  $N(\text{H I})$ - $N(\text{C IV})$  scatter plot. The blue points correspond to the sub-sample of 22 systems with secure H I measurements, while the components from other absorbers are shown in grey. The green upper limit with error-bar for  $N(\text{C IV})$  corresponds to the  $z_{\text{abs}} = 0.00218$  absorber towards SBS 1108+560 that does not have a H I detection. The dashed line represents  $N(\text{H I}) = N(\text{C IV})$ , and the solid line corresponds to  $N(\text{H I}) = 10^{17.2} \text{ cm}^{-2}$  that distinguishes Lyman Limit Systems (LLS) from sub-LLS. The brown points correspond to free-fits of H I in the  $z_{\text{abs}} = 0.09763$  system towards SDSS J135712.61+170444.1 with Ly $\alpha$  that is heavily contaminated with Galactic C II 1334. Bottom: The distribution of Doppler  $b$ -parameter and column density for the C IV components, which show large scatter.

density for this absorber. The  $z_{\text{abs}} = 0.09763$  system towards SDSS J135712.61+170444.1 has Ly $\alpha$  that is heavily contaminated with the Galactic C II 1334 and therefore we do not use the  $N(\text{H I})$  for these components in the ionization modelling. One out of 3 C IV components in the  $z_{\text{abs}} = 0.08940$  system towards QSO B1435-0645 is saturated, and we have excluded it from analysis in this paper.

The  $b(\text{C IV})$ - $N(\text{C IV})$  relationship has a Spearman rank test<sup>8</sup>  $p$ -value of  $\ll 0.001$  for null hypothesis (that there is no correlation), and the correlation coefficient of  $r = 0.47$  (bottom-panel, Fig. 3), but there is significant scatter. It is comparatively more difficult to detect lines with low  $N$  and high  $b$  at  $\geq 3\sigma$  level due to noise. This is the reason for paucity of points in the upper-left region of Fig. 3. It should be noted that the aforementioned trend can also be an artifact of this.

We however do find strong correlations ( $r \gtrsim 0.7$ ) between ab-

<sup>8</sup> We are using Spearman rank test throughout the paper instead of Pearson test because it is agnostic to the order, unlike the latter which specifically tests for linear trends. A  $p < 0.003$  implies  $> 3\sigma$  significance level.

**Table 2.** Basic properties of the C IV absorbers

QSO (1)	$z_{\text{em}}$ (2)	$z_{\text{abs}}$ (3)	Heavier Metals (4)	Low Ions (5)	High Ions (6)	No. of HI (7)	No. of C IV (8)	$\log[\Sigma N(\text{C IV}) (\text{cm}^{-2})]$ (9)
1H 1613-097	0.33500	0.06274	N	N	N	2	2	13.48
2MASS J10155924-2748289	0.24125	0.00819	Y	Y	N	3	3	14.18
3C 263	0.39758	0.06355 <sup>F</sup>	Y	Y	N	4	3	14.06
3C 263	0.39758	0.11391 <sup>*F</sup>	Y	N	Y	3	1	13.35
FBQS 0751+2919	0.91572	0.06020 <sup>D</sup>	Y	N	N	5	3	13.66
HE 0056-3622	0.16298	0.04344 <sup>F</sup>	N	N	N	2	1	13.59
HE 0439-5254	1.05300	0.00546 <sup>H</sup>	N	N	N	4	3	13.97
IRAS F00040+4325	0.16363	0.12247 <sup>*</sup>	Y	N	Y	2	2	13.73
IRAS F04250-5718	0.10457	0.00377	Y	Y	N	4	2	12.88
J141949.39+060654.0	1.64890	0.04872	Y	Y	Y	3	2	14.45
LBQS 0107-0235	0.95703	0.11548 <sup>*</sup>	Y	N	N	2	2	14.22
LBQS 1435-0134	1.30791	0.13842 <sup>*D</sup>	Y	N	Y	1	1	13.50
PG 0003+158	0.45047	0.09106 <sup>*F</sup>	N	N	N	3	2	13.84
PG 0832+251	0.32865	0.01749 <sup>HF</sup>	Y	Y	N	6	6	14.74
PG 0953+414	0.22312	0.06808 <sup>*EF</sup>	N	N	N	2	1	13.72
PG 1116+215	0.17466	0.13850 <sup>*F</sup>	Y	Y	Y	1 <sup>A</sup>	1	13.12
PG 1148+549	0.97598	0.00346 <sup>D</sup>	N	N	N	2	1	13.59
PG 1202+280	0.16530	0.05144 <sup>H</sup>	Y	Y	N	3	1	13.66
PG 1216+069	0.33243	0.12360 <sup>*F</sup>	Y	N	Y	4	4	14.29
PG 1222+216	0.43460	0.05456 <sup>F</sup>	Y	N	N	3	2	13.65
PG 1222+216	0.43460	0.09870 <sup>F</sup>	N	N	N	1	1	13.99
PG 1352+183	0.15200	0.09407	N	N	N	3	3	13.99
PG 1407+265	0.94000	0.07225 <sup>*D</sup>	N	N	N	2	2	13.67
PG 1424+240	0.60100 <sup>B</sup>	0.12119 <sup>*F</sup>	Y	Y	Y	2	2	13.77
PG 1424+240	0.60100 <sup>B</sup>	0.14702 <sup>*F</sup>	Y	Y	Y	4	2	14.15
PG 1522+101	1.32801	0.07519 <sup>*D</sup>	Y	N	Y	1	1	13.38
PHL 1811	0.19168	0.08093 <sup>EF</sup>	Y	Y	N	2	2	13.89
PHL 1811	0.19168	0.13542 <sup>*F</sup>	N	N	N	1	1	13.14
PHL 2525	0.19975	0.06668 <sup>F</sup>	Y	N	N	2	1	13.72
PKS 1302-102	0.27840	0.00439 <sup>EF</sup>	Y	N	N	1	1	12.94
PMN J1103-2329	0.18617	0.00400 <sup>HF</sup>	Y	N	N	2	1	14.06
PMN J1103-2329	0.18617	0.08354 <sup>F</sup>	Y	Y	N	3	2	14.18
Q 2251+155	0.85900	0.05054 <sup>*</sup>	N	N	N	1	1	13.40
Q 2251+155	0.85900	0.15373	Y	Y	N	4	2	14.17
QSO B1435-0645	0.12900	0.08940	Y	N	Y	4	3	14.17 <sup>G</sup>
RBS 1666	0.07963	0.04235	Y	Y	N	2	2	13.94
RXJ 1230.8+0115	0.11642	0.00574	Y	Y	N	2	2	13.25
RXJ 1230.8+0115	0.11642	0.07810	Y	N	Y	2	2	14.31
RXJ 1230.8+0115	0.11642	0.09513 <sup>*+</sup>	N	N	N	2	1	13.05
RXJ 2154.1-4414	0.34366	0.06229 <sup>F</sup>	Y	Y	Y	2	2	14.43
SBS 1108+560	0.76662	0.00218 <sup>HF</sup>	Y	Y	N	0	2	14.51
SBS 1122+594	0.85142	0.00402 <sup>HF</sup>	Y	Y	N	1	1	14.49
SBS 1122+594	0.85142	0.06016 <sup>F</sup>	Y	N	N	2	1	13.50
SDSS J004222.29-103743.8	0.42312	0.09509 <sup>H</sup>	Y	Y	Y	5	3	14.76
SDSS J021218.32-073719.8	0.17194	0.01594	Y	Y	N	2	2	14.25
SDSS J082633.51+074248.3	0.30956	0.05126 <sup>H</sup>	Y	Y	N	2	1	14.11
SDSS J084349.49+411741.6	0.99079	0.03016 <sup>*+H</sup>	Y	N	N	1	1	13.83
SDSS J091029.75+101413.6	0.46141	0.14237	Y	Y	N	3	2	14.19
SDSS J092554.43+453544.4	0.32948	0.01422 <sup>HF</sup>	N	N	N	3	2	13.50
SDSS J094952.91+390203.9	0.36347	0.01815 <sup>HF</sup>	Y	N	N	3	3	14.62
SDSS J095915.65+050355.1	0.16230	0.05901 <sup>H</sup>	Y	Y	N	3	3	14.69
SDSS J104741.75+151332.2	0.38508	0.00231 <sup>*</sup>	Y	Y	N	2	2	13.89
SDSS J105945.23+144142.9	0.63171	0.00243 <sup>*D</sup>	Y	Y	Y	4	1	14.05
SDSS J105958.82+251708.8	0.66191	0.11884 <sup>D</sup>	Y	N	N	2	1	14.32
SDSS J110406.94+314111.4	0.43336	0.06209 <sup>D</sup>	N	N	N	2	1	14.23
SDSS J111754.31+263416.6	0.42047	0.04751 <sup>D</sup>	Y	Y	N	2	2	14.31
SDSS J112244.89+575543.0	0.90685	0.05324 <sup>D</sup>	Y	N	N	2	1	13.75
SDSS J121037.56+315706.0	0.39018	0.05983 <sup>D</sup>	Y	Y	Y	1	1	14.20
SDSS J121037.56+315706.0	0.39018	0.07812 <sup>*D</sup>	N	N	N	2	2	13.66
SDSS J121114.56+365739.5	0.17075	0.07779 <sup>D</sup>	N	N	N	2	2	14.10
SDSS J123604.02+264135.9	0.20789	0.06163 <sup>H</sup>	Y	Y	N	2	1	14.23
SDSS J124511.25+335610.1	0.71170	0.00222 <sup>*</sup>	N	N	N	1	1	13.39
SDSS J133053.27+311930.5	0.24252	0.03413 <sup>H</sup>	Y	Y	N	2	2	14.26

QSO (1)	$z_{\text{em}}$ (2)	$z_{\text{abs}}$ (3)	Heavier Metals (4)	Low Ions (5)	High Ions (6)	No. of H I (7)	No. of C IV (8)	$\log[\Sigma N(\text{C IV}) (\text{cm}^{-2})]$ (9)
SDSS J134206.56+050523.8	0.26387	0.13989 <sup>*D</sup>	Y	Y	N	4	2	14.46
SDSS J134251.60-005345.3	0.32396	0.07155 <sup>*D</sup>	Y	Y	N	2	2	13.89
SDSS J135712.61+170444.1	0.15084	0.08364 <sup>DF</sup>	Y	N	N	2	1	13.79
SDSS J135712.61+170444.1	0.15084	0.09763 <sup>DF</sup>	Y	Y	Y	6 <sup>C</sup>	5	14.06
SDSS J161916.54+334238.4	0.46853	0.14133 <sup>*DH</sup>	Y	N	N	2	1	13.75
VII Zw 244	0.13089	0.00235 <sup>H</sup>	Y	Y	N	1	1	13.38

(1) QSO name; (2) Emission redshift is based on the intrinsic Ly $\alpha$  emission, or taken from NASA/IPAC Extragalactic Database (NED) if Ly $\alpha$  isn't covered by COS; (3) Absorber redshift; (4) Presence of metal species other than C II and C IV; (5) Detection of at least one low ion (C II, Si II, N II); (6) Detection of at least one high ion (N V, O VI); (7) No. of H I components; (8) No. of C IV components; (9) Combined  $N(\text{C IV})$  of components based on Voigt profile fits.

<sup>\*</sup>The  $N(\text{H I})$  is well constrained for these absorbers for at least one component. <sup>†</sup>The Ly $\alpha$  is saturated but the  $N(\text{H I})$  is well constrained (see Sec. 4.1).

<sup>A</sup>The  $b(\text{H I})$  and  $N(\text{H I})$  are adopted from Sembach et al. (2004); <sup>B</sup>The emission redshift is taken from Rovero et al. (2016); <sup>C</sup>The H I is heavily contaminated with Galactic C II  $\lambda 1334$ ; <sup>D</sup>The systems overlap with Burchett et al. (2015); <sup>E</sup>The systems overlap with Cooksey et al. (2010); <sup>F</sup>The systems overlap with Danforth et al. (2016); <sup>G</sup>The saturated C IV component in this absorber is excluded here; <sup>H</sup>The systems are around targeted galaxies.

**Table 3.** Summary of the line measurements

Median redshift	0.062
Maximum $\Delta Z$ for C IV	20.2
Systems	69
C IV components	127 <sup>*</sup>
H I components	168
Systems with heavier metals than carbon	52 (75%)
Systems with low ions	32 (46%)
Systems with high ions	16 (23%)
$b(\text{C IV}) (\text{km s}^{-1})$	4 – 44
$b(\text{H I}) (\text{km s}^{-1})$	4 – 81
$\log[N(\text{C IV}) (\text{cm}^{-2})]$	12.31 – 14.69
$\log[N(\text{H I}) (\text{cm}^{-2})]$	12.91 – 18.09

Note: The column density ranges mentioned here are for *individual* components. The range of  $b$  and  $N$  listed for H I encompass all systems in the sample, though reliable profile fits for H I are available only for 32% of the absorbers (22/69) with the Ly $\alpha$  saturation affecting measurements in the remaining systems. <sup>\*</sup>This includes the saturated C IV component.

sorption strengths based on AOD measurements and  $\Delta v_{90}$  for both C IV and H I (Fig. 4). Here the values are based on entire absorption in the system. It should be noted that by H I and C IV we mean Ly $\alpha$  and C IV  $\lambda 1548$ , respectively. Since many of the H I absorptions are saturated, we only use the sample with secure H I in the  $N(\text{H I}) - \Delta v_{90}(\text{H I})$  relation. The  $W_r - \Delta v_{90}$  correlations are strong for both C IV ( $r = 0.79$ ) and H I ( $r = 0.94$ ), and the  $N - \Delta v_{90}$  is correlated similarly for both ions ( $r = 0.70$  for C IV and  $r = 0.89$  for H I) ( $p \ll 0.001$  for all). We use the HYPER-FIT package<sup>9</sup> (Robotham & Obreschkow 2015) to fit linear models to these relations by optimizing likelihood of data for a Gaussian distribution about the model, using the Nelder-Mead method (Nelder & Mead 1965). It takes into account the uncertainties in the data as well. The dashed lines in Fig. 4 represent  $1\sigma$  scatter. The scaling relationships are

$$W_r(\text{C IV}) = (4.46 \pm 0.36)\Delta v_{90}(\text{C IV}) - (117.21 \pm 30.03), \quad (4)$$

$$W_r(\text{H I}) = (5.09 \pm 0.30)\Delta v_{90}(\text{H I}) - (128.51 \pm 47.95), \quad (5)$$

$$\log N(\text{C IV}) = (2.18 \pm 0.24) \log \Delta v_{90}(\text{C IV}) + (9.82 \pm 0.43), \quad (6)$$

$$\log N(\text{H I}) = (1.72 \pm 0.20) \log \Delta v_{90}(\text{H I}) + (10.70 \pm 0.40). \quad (7)$$

If we exclude the two outliers in  $W_r(\text{H I}) - \Delta v_{90}(\text{H I})$  scatter, the

slope and intercept of the fit change to  $5.20 \pm 0.14$  and  $-119.39 \pm 21.03$ , respectively. Such relationships confirm that observed  $W_r$  is a stronger function of absorption width than  $N$ . Given that there are more H I components in a system compared to C IV, it suggests that C IV bearing H I components may dominate equivalent widths compared to the ones without C IV, which typically tend to have lower  $N(\text{H I})$ . Interestingly, slopes and intercepts in these relationships are similar even though they correspond to different elements. Broadly this suggests that the H I and C IV ions reside in gas of similar physical conditions. The absence of  $N(\text{H I}) - \Delta v_{90}(\text{H I})$  correlation in Lehner et al. (2018) is mainly because they were also including saturated systems with  $N(\text{H I}) > 10^{15} \text{ cm}^{-2}$ . Moreover, their sample was H I-selected unlike our sample which is C IV-selected. Absorbers with detectable amounts of metals could be probing a smaller range of astrophysical environments than a sample of H I absorbers unbiased by the presence of metals.

Fig. 5 shows the distributions of the C IV absorption properties. As seen in the *top-left* panel, the system redshifts have a median at  $\approx 0.062$ . The  $N(\text{C IV})$  values (*top-right* panel) range from  $10^{12.3} - 10^{14.7} \text{ cm}^{-2}$  and peak at  $\sim 10^{13.4} \text{ cm}^{-2}$ . One expects a decline in the number of detections with increasing column density since large C IV column density systems are likely to be part of optically thick Lyman limit and damped Lyman-alpha absorbers, whose redshift number densities are lower compared to metal absorbers tracing more diffuse gas belonging to the CGM and IGM. The rise till  $N(\text{C IV}) \approx 10^{13.4} \text{ cm}^{-2}$  is an artifact of the overall sensitivity of the spectra. Pathlengths are expected to saturate for high column densities of  $N(\text{C IV}) \gtrsim 10^{15.0} \text{ cm}^{-2}$ . From Table 1, it seems that pathlengths are going to saturate around  $\approx 20.2$  and therefore we can approximate completeness as  $\approx 100\%$  at  $N(\text{C IV}) = 10^{14.9} \text{ cm}^{-2}$ . Based on this, the completeness level is 55% at  $N(\text{C IV}) = 10^{13.4} \text{ cm}^{-2}$ . Hence, the number of C IV detections at the  $\geq 3\sigma$  confidence is expected to increase till such  $N(\text{C IV})$  and decline at higher column densities.

Fig. 5 also shows the distribution of Doppler  $b$  parameters for the C IV components obtained from the profile fitting. The median  $b(\text{C IV})$  is  $\sim 14 \text{ km s}^{-1}$ , corresponding to a temperature of  $T \leq 1.4 \times 10^5 \text{ K}$ ; assuming no turbulent broadening. There are 74 components with  $b(\text{C IV}) \geq 12 \text{ km s}^{-1}$ , corresponding to temperature upper limits of  $T \gtrsim 10^5 \text{ K}$ . Six C IV absorbers in our sample also show O VI, which is a better tracer of warm collisionally ionized gas than C IV. The bottom panel of Fig. 5 shows the distribution of the velocity widths of the C IV profiles. The C IV absorption is spread over a range of velocities from as low as  $\approx 17 \text{ km s}^{-1}$  up to  $\approx 167 \text{ km s}^{-1}$  with the median at  $\approx 64 \text{ km s}^{-1}$ . There are no ab-

<sup>9</sup> <https://hyperfit.icrar.org>

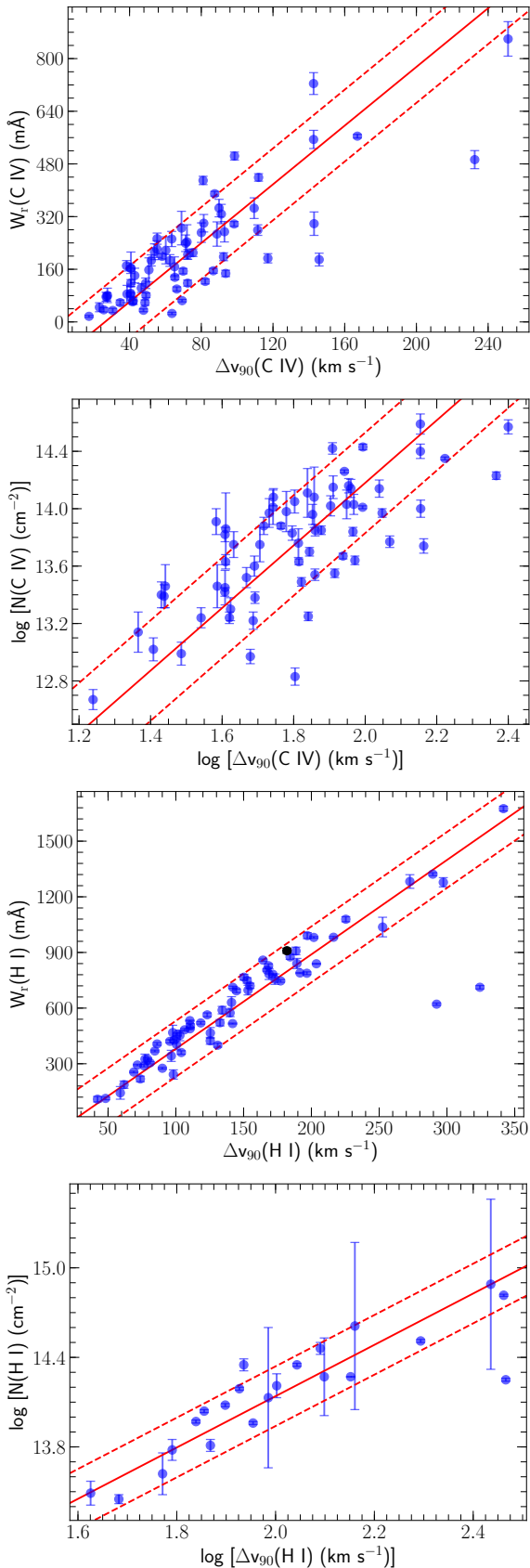


**Figure 4.** Correlations between line strengths of H I and C IV with the  $\Delta v_{90}$  based on AOD integration for the entire profile. The  $W_r(\text{H I})$  of Ly $\alpha$  in  $z = 0.09763$  absorber (black circle) is heavily contaminated by Galactic C II 1334 Å. The bottom panel only shows the sample with secure H I.

sorptions with  $\Delta v_{90} > 170 \text{ km s}^{-1}$  which implies that, unlike the population of C IV absorbers in the high- $z$  Universe (Lehner et al. 2014), kinematically broad C IV absorbers are rare in the present Universe.

For the secure sample, the temperatures derived from the different  $b$ -values of H I and C IV are such that almost all but one of the clouds have  $T < 10^5 \text{ K}$ , with the median at  $T \sim 10^{4.2} \text{ K}$  (Fig. 6). The *middle* panel of Fig. 6 shows the aligned H I and C IV components spread between two extreme scenarios of exclusively thermal and fully turbulent broadening. This would also mean that the C IV absorbers (of the secure sample at least) are predominantly tracing relatively cooler ( $T \sim 10^4 \text{ K}$ ) gas, with photoionization being the dominant ionizing mechanism. A comparison of non-thermal ( $b_{\text{nt}}$ ) and thermal ( $b_{\text{t}}$ ) broadening in the C IV reveals that turbulence has a higher contribution (bottom panel of Fig. 6). The median  $b_{\text{nt}}$  and  $b_{\text{t}}$  are  $11 \text{ km s}^{-1}$  and  $5 \text{ km s}^{-1}$ , respectively. This is lesser than the median  $b_{\text{nt}}$  for photoionized O VI absorbers by  $12 \text{ km s}^{-1}$  (Savage et al. 2014). The relationship between  $b_{\text{nt}}$  and environment is explored in Sec. 7.

### 4.3 Correlations between ions

Ions of different elements with similar ionization potentials are uniformly influenced by the ionizing radiation and hence can be used to assess the relative chemical abundances in the absorber. For example, in the photoionization models, the observed column densities of C II, O II, Mg II, and Si II are routinely used to estimate the relative abundances as these four species have comparable creation and destruction energies. Observed column densities of well aligned ions of the same element, or different elements, tracing the same phase will exhibit a certain amount of correlation in their observed column densities. By the same token, a weak correlation between column densities of different ions of the same element can be an indication of their preference for different gas phases. Also, a weak correlation between low ions or between high ions of different elements can be suggestive of differences in elemental abundances across the sample.

In Fig. 7, Fig. 8 and Fig. 9 we investigate the relations amongst the C and Si ions, which have a higher detection rate in the sample compared to ions of other elements. In a number of cases, C II, Si II and Si III are non-detections, yielding useful upper limits on the column densities. We determine the bisector regression fits to the column density correlations by taking into account these censored values also, in addition to the detections, by using the survival analysis statistical package ASURV<sup>10</sup> (Feigelson & Nelson 1985; Isobe et al. 1986). The Schmitt's binning method is used (Schmitt 1985) since it is the only method in ASURV capable of handling censoring in both the independent and dependent variables. The fits are based on convergence after 10000 iterations. Fig. 7 shows the relations between C and Si ions with C IV. The linear fits imply

$$\log N(\text{C II}) = (1.46 \pm 0.14) \log N(\text{C IV}) - (6.72 \pm 1.94), \quad (8)$$

$$\log N(\text{Si II}) = (1.13 \pm 0.13) \log N(\text{C IV}) - (2.75 \pm 1.70), \quad (9)$$

$$\log N(\text{Si III}) = (1.65 \pm 0.18) \log N(\text{C IV}) - (9.90 \pm 2.49), \quad (10)$$

$$\log N(\text{Si IV}) = (1.05 \pm 0.08) \log N(\text{C IV}) - (1.65 \pm 1.13). \quad (11)$$

The least scatter is for the Si IV - C IV relation. This is expected since the ionization energy for C IV is closest to that for Si IV amongst the four ions. However, the scatter only slightly increases with increasing difference in ionization potential suggesting that the C IV

<sup>10</sup> <http://python-asurv.sourceforge.net/>



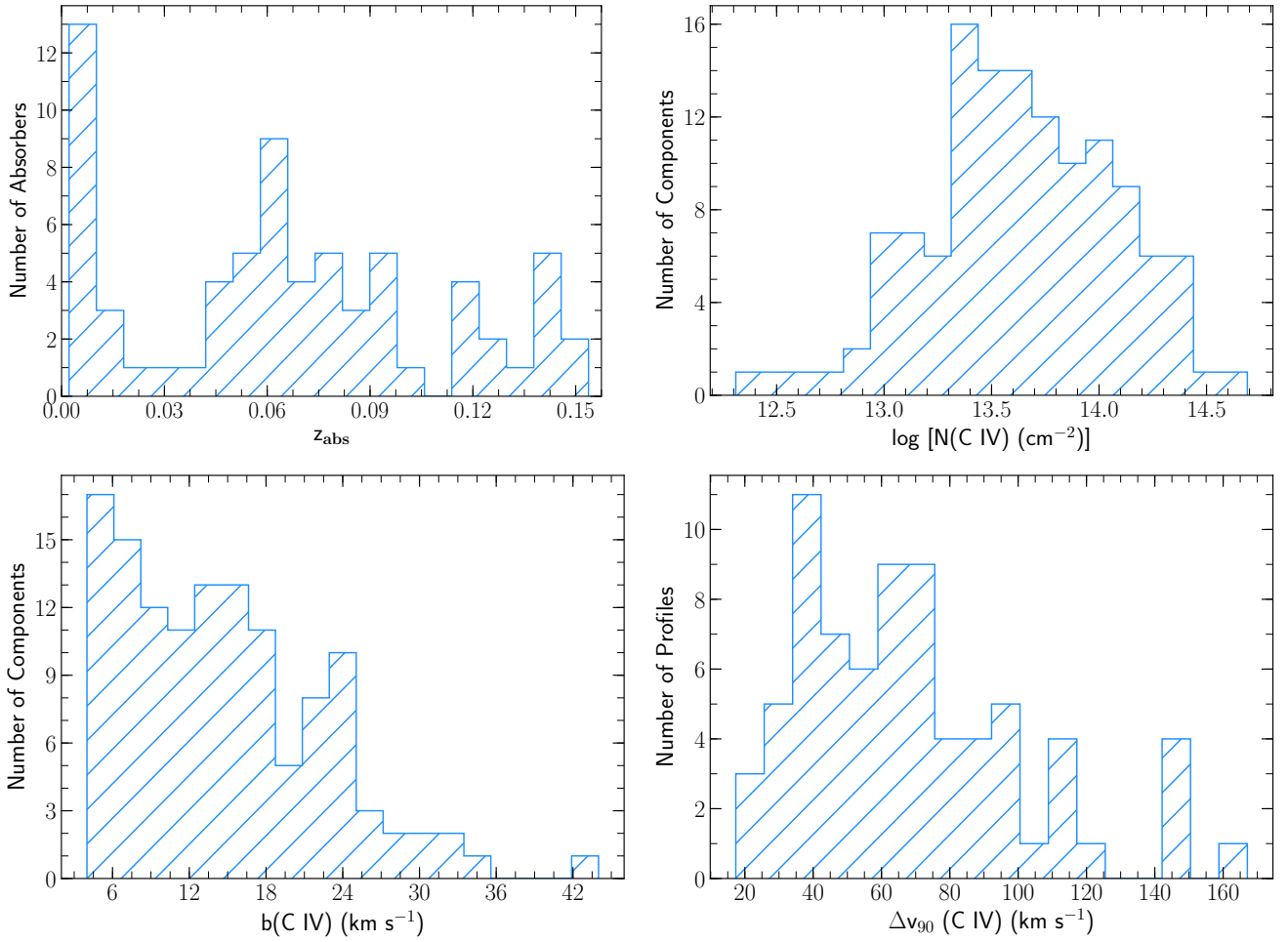


**Figure 5.** Top left-hand panel: The distribution of absorber redshifts. Top right-hand panel: The column density distribution of C IV components. Bottom left-hand panel: The distribution of Doppler parameter for C IV components. Bottom right-hand panel: The distribution of velocity width containing 90% of the flux in C IV absorption line profiles.

and lower ions may not always represent vastly different gas phases. Ionization models often show that absorbers where the low ions are a non-detection can be explained with a single C IV phase. Instances where the low ions are a detection, the C II (along with similar low ions) and C IV can be explained by considering photoionized gas within a narrow density range (Lopez et al. 1999; Manuwal et al. 2019). In certain absorbers C IV requires a separate phase, especially when the kinematic profiles of the low and high ions differ from each other (Ding et al. 2003; Misawa et al. 2008). However, unlike O VI and Ne VIII absorbers which trace distinctly different density-temperature zones from the low ions, the predictions from ionization models for C II and C IV often indicate origin in a medium where ionization levels are not vastly different. A similar trend of weakening of correlation with increasing differences in ionization potential is also seen by Burchett et al. (2015). The trends amongst the low and high ions of Si are explored in Fig. 8 and the linear fits suggest

$$\log N(\text{Si II}) = (0.69 \pm 0.09) \log N(\text{Si III}) + (3.99 \pm 1.10), \quad (12)$$

$$\log N(\text{Si III}) = (1.63 \pm 0.16) \log N(\text{Si IV}) - (7.85 \pm 2.11), \quad (13)$$

$$\log N(\text{Si II}) = (1.00 \pm 0.18) \log N(\text{Si IV}) - (0.08 \pm 2.29). \quad (14)$$

The scatter in Si III - Si IV is slightly lower than that in Si II - Si IV because of the closer ionization conditions between the former pair of species. The creation and destruction energies of C II

(11 eV/24 eV) fall in between the corresponding values for Si II and Si III (8 eV/16 eV/33 eV). In Fig. 9 we compare the column densities of these ions with C II. The survival analysis yields

$$\log N(\text{C II}) = (1.59 \pm 0.21) \log N(\text{Si II}) - (6.79 \pm 2.62), \quad (15)$$

$$\log N(\text{C II}) = (0.86 \pm 0.11) \log N(\text{Si III}) + (2.47 \pm 1.38). \quad (16)$$

The C II is comparably well correlated with Si III and Si II. In ionization models, all three species are often identified as originating from gas of similar density. In fact, surveys of Mg II absorbers at  $z < 0.4$  often use C II and Si II as proxy doublets for Mg II because of their origin in a common phase (e.g. Narayanan et al. 2005; Muzahid et al. 2018).

## 5 ABSORBER LINE STATISTICS

Here we determine the column density distribution function and the contribution of C IV absorbers to the closure density where the statistics are based on *total* column densities of systems as per VPFIT, as opposed to AOD based integrated column densities. We exclude the 16 systems that were found around targeted galaxies, and the  $z_{\text{abs}} = 0.08940$  system towards QSO B1435-0645 that has a saturated C IV component.

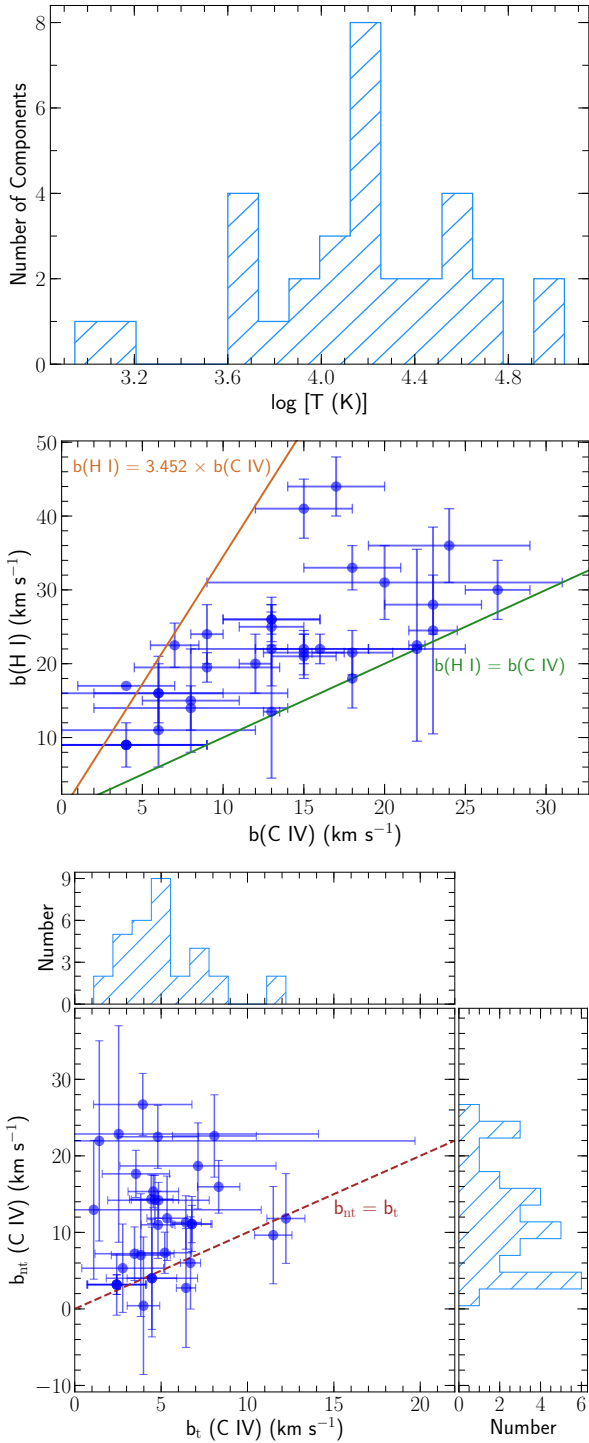


**Figure 6.** Top: Temperatures in the C IV absorbers inferred from the  $b$ -values of (H I) and (C IV). Here we consider only the sub-sample with secure H I measurements. Middle: The  $b(\text{H I}) - b(\text{C IV})$  relation for the sub-sample with secure H I. The steeper solid-brown line represents the relation between  $b(\text{H I})$  and  $b(\text{C IV})$  when the line broadening is purely thermal, and the solid-green line marks line broadening that is purely non-thermal. Bottom: The  $b_{\text{nt}}-b_{\text{t}}$  scatter plot with histograms for C IV in the middle panel. The dashed line represents  $b_{\text{nt}} = b_{\text{t}}$ .

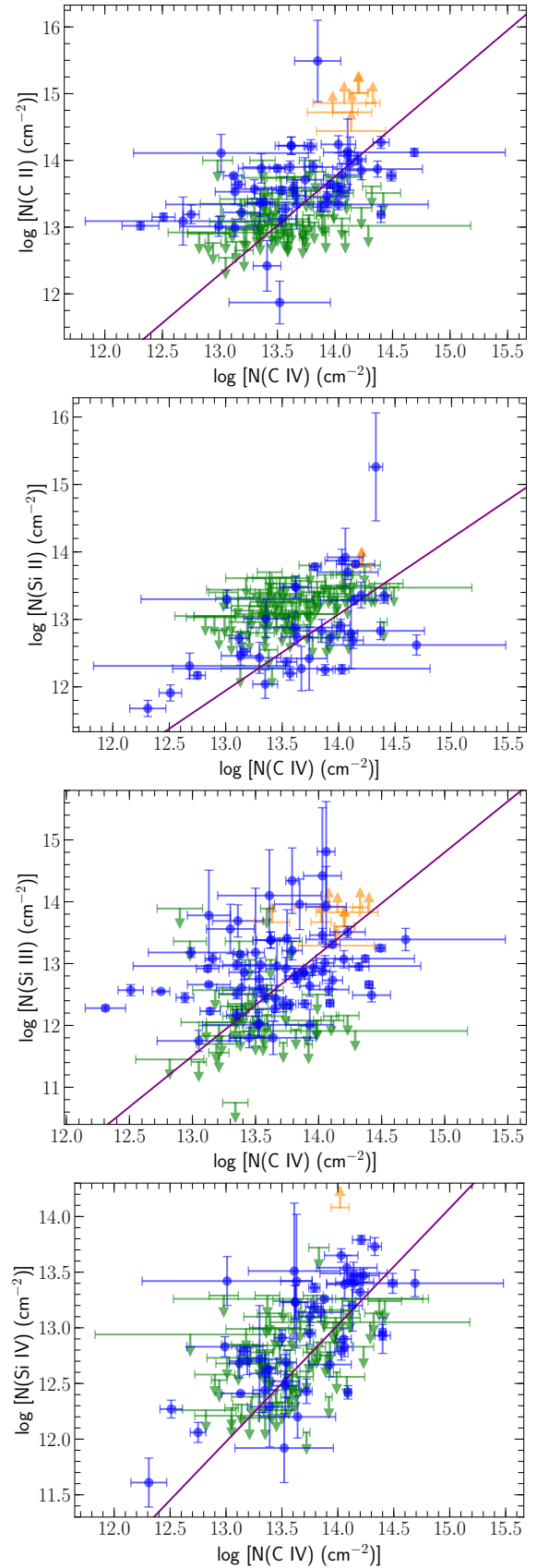


**Figure 7.** Column densities of different ions plotted against C IV. The green arrows represent  $3\sigma$  upper limits from non-detections and the orange arrows are lower limits for saturated components. The solid line in each panel corresponds to best-fit relations that are based on survival analysis, including the censored data i.e. upper and lower limits.

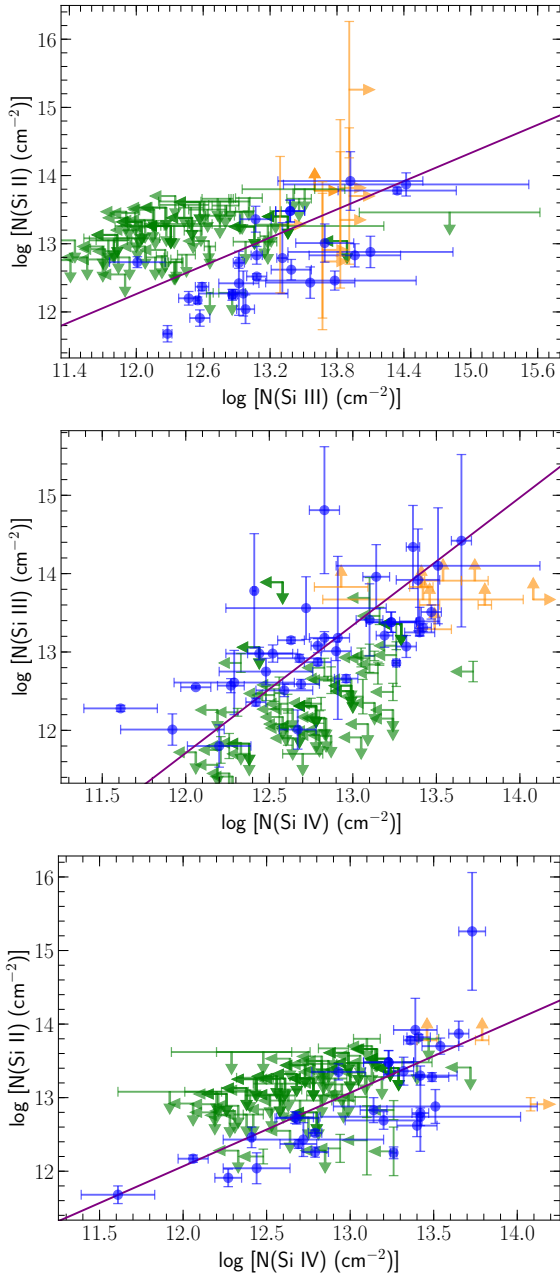


**Figure 8.** The column density trends of different ions plotted against Si IV. The green arrows represent  $3\sigma$  upper limits from non-detections and the orange arrows are lower limits for saturated components. The solid line in each panel correspond to correlations between the column densities, including the data points which are upper and lower limits.

### 5.1 Column density distribution function

The column density distribution function  $f(N(\text{C IV}))$  is the distribution of number of absorbers  $\mathcal{N}(N(\text{C IV}))$  in each C IV column density bin  $\Delta N(\text{C IV})$  normalized by the comoving path length  $\Delta X(N(\text{C IV}))$  for that column density threshold. The normalization is to correct for the completeness at each column density. This is determined as

$$f(N(\text{C IV})) = \frac{\mathcal{N}(N(\text{C IV}))}{\Delta N(\text{C IV})\Delta X(N(\text{C IV}))}. \quad (17)$$

In order to determine the comoving path lengths, we first convert each wavelength in our spectra to redshift, and then from redshift to

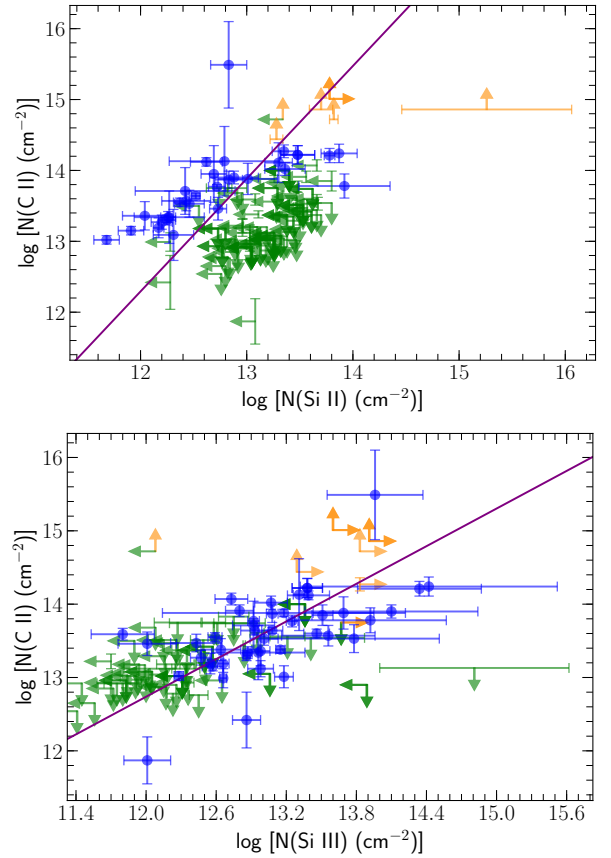


**Figure 9.** The column density trends of C II with Si II and Si III. The green arrows represent  $3\sigma$  upper limits from non-detections and the orange arrows are lower limits for saturated components. The solid line in each panel correspond to correlations between the column densities, including the data points which are upper and lower limits.

$X$  as

$$X(z) = \frac{2}{3\Omega_m} [\sqrt{(1+z)^3\Omega_m + \Omega_\Lambda} - 1]. \quad (18)$$

The subtraction by 1 in Eq. 18 is to account for the fact that  $X(0) = 0$ . The total comoving path length for each column density is determined with a procedure analogous to that for the redshift path length (Sec. 3). The values are provided in Table 1.

The  $f(N(\text{C IV}))$  for our absorbers with column density bins of  $\Delta \log N(\text{C IV}) = 0.2$  dex is shown in Fig. 10. The error is determined by adding two sources of error in quadrature. The first is the contribution from Poisson uncertainty in  $\mathcal{N}(N(\text{C IV}))$ , which is the primary source of error. Another contribution is from the uncertainty in comoving path length (Danforth & Shull 2008)

$$\delta \Delta X_i = \frac{\Delta X_{i+1} - \Delta X_{i-1}}{8}, \quad (19)$$

where  $\Delta X_{i\pm 1}$  corresponds to co-moving pathlength for  $\log N(\text{C IV}) \pm 0.1$ . The Spearman rank test for  $f(N(\text{C IV})) - N(\text{C IV})$  relation gives  $r \sim -1$ ,  $p \ll 0.001$  and the function can be modelled accurately with a power law given by the optimum likelihood fit using HYPER-FIT as

$$f(N(\text{C IV})) = k \left[ \frac{N(\text{C IV})}{N_0} \right]^\alpha, \quad (20)$$

where  $N_0 = 10^{14} \text{ cm}^{-2}$ ,  $\log k = -14.18 \pm 0.08$  and  $\alpha = -1.24 \pm 0.13$ .

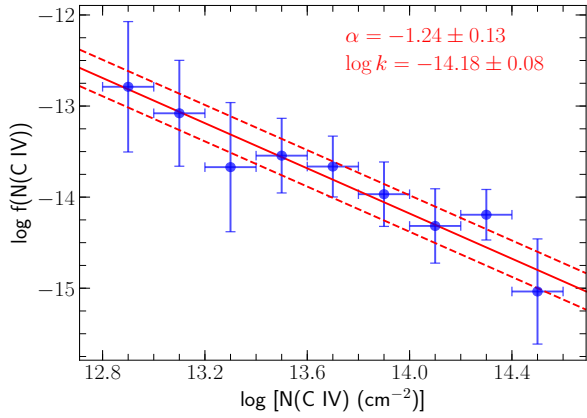


**Figure 10.** The column density distribution function for the C IV sample. The solid-red line is the power-law fit of Eq. 20 and the dashed lines show its  $1\sigma$  uncertainty.

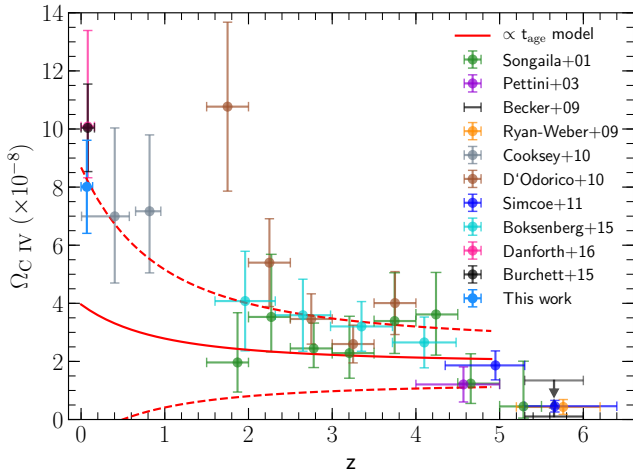


**Figure 11.** This shows various estimates from previous surveys along with this one (shown in light-blue) for the ratio of mass density in C IV relative to the critical density for a flat universe from high- $z$  to the present. The solid-red curve is the best-fit model given by Cooksey et al. (2010) (see their Eq. 23) for linear evolution in  $\Omega_{\text{C IV}}$  with age of the universe, based on the C IV mass density values for  $1 < z < 5$ . The dashed curves show  $1\sigma$  region for the same. The model extended to lower redshifts shows that the mass-density of C IV has steadily increased from high redshifts to the present.

This  $k$  is within  $1\sigma$  of  $-14.06^{+0.15}_{-0.16}$  for  $\langle z \rangle = 0.40227$  from  $G=1+2$  sample in Cooksey et al. (2010), but not consistent with  $-13.76 \pm 0.07$  in Burchett et al. (2015). The power-law index  $\alpha$  is also significantly higher than  $-2.07 \pm 0.15$  in Burchett et al. (2015), but consistent within  $2\sigma$  with  $-1.74^{+0.28}_{-0.31}$  in Cooksey et al. (2010). However, Burchett et al. (2015) used their gamma-function fit instead of the power-law fit for analysis. The column density distribution function is a crucial parameter in the estimation of the mass density contribution from C IV absorbers to the critical density. As the distribution function shows, the low column density absorbers are far more numerous compared to the high column density systems. Constraining the distribution function accurately at lower column densities hence becomes important. As shown in Fig. 10, the distribution function arrived at in Eq. 20 explains well the column density trend across three orders of magnitude.

## 5.2 C IV density parameter ( $\Omega_{\text{C IV}}$ )

The absorber line density above a certain limiting column density  $N_{\text{lim}}$  is defined as

$$\frac{dN}{dX}(N(\text{C IV}) \geq N_{\text{lim}}) = \int_{N_{\text{lim}}}^{\infty} f(N(\text{C IV})) dN(\text{C IV}). \quad (21)$$

We use the model for  $f(N(\text{C IV}))$  in Eq. 20 to determine the  $dN/dX$ . The observed lower limit of  $N(\text{C IV})$  in the systems is  $N_{\text{lim}} = 10^{12.9} \text{ cm}^{-2}$  and that gives  $dN/dX = 5.1 \pm 1.0$ . The uncertainty is determined by considering the  $1\sigma$  scatter provided by HYPER-FIT. This value is  $\sim 2.7$  times higher than the prediction for this epoch based on the linear evolution model by Hasan et al. (2020). They mention that such discrepancies could either be due to the lack of measurements for high redshifts, or a sudden increase in C IV clouds at  $z \sim 0.5$  over a 0.5 Gyr time period, but argue against the latter, as it is difficult to understand such a rapid evolution.

$\Omega_{\text{C IV}}$  is the ratio of the mass density of C IV to the critical density  $\rho_c$  of the Universe. We can use the column density distribution for our sample to estimate this for the redshift range of our absorbers as

$$\Omega_{\text{C IV}} = \frac{H_0 m_c}{c \rho_{c,0}} \int_{N_{\text{min}}}^{N_{\text{max}}} f(N(\text{C IV})) N(\text{C IV}) dN(\text{C IV}), \quad (22)$$

where  $H_0$  is Hubble parameter for the present Universe,  $m_c$  is the mass of carbon atom,  $\rho_{c,0} = 3H_0^2/8\pi G$  is the present-day value of the critical density,  $c$  is the speed of light in vacuum, and  $N_{\text{min}}$  and  $N_{\text{max}}$  are the integration limits. On taking  $N_{\text{min}}, N_{\text{max}} = 10^{12.9}, 10^{15.0} \text{ cm}^{-2}$  (to be consistent with Burchett et al. 2015 and Danforth et al. 2016), we arrive at  $\Omega_{\text{C IV}} = (8.01 \pm 1.62) \times 10^{-8}$ .

Fig. 11 shows the value of  $\Omega_{\text{C IV}}$  at different redshifts reported by previous surveys from  $z = 6$  to the present, along with our estimate. These values are corrected for cosmology according to the scaling method described in Cooksey et al. (2010). Becker et al. (2009) provide lower and upper limits at  $z > 5.3$  instead of a measurement. Our estimate based on the fit is consistent with the value reported by Cooksey et al. (2010) within  $1\sigma$ . Cooksey et al. (2010) had derived a model for linear evolution of  $\Omega_{\text{C IV}}$  with the age of the Universe based on  $1 < z < 5$ . Our estimate is well within its prediction for the low- $z$  Universe, which suggests a steady increase of mass-density across time. It is also consistent with Burchett et al. (2015) who used their column density distribution function for  $z < 0.16$  to estimate the density parameter, and Danforth et al. (2016) who used a differential distribution ( $\partial^2 N(N)/\partial \log N \partial z$ ) of their sample to arrive at the mass-density estimate.

The mass density in C IV is roughly a constant from  $z \sim 5 - 1$  (Pettini et al. 2003; Boksenberg & Sargent 2015) despite the cosmic star formation rate density and the activity of bright AGNs peaking at  $z \sim 2$  (Boyle et al. 2000; Madau & Dickinson 2014). The hydrodynamic simulations of Oppenheimer & Davé (2006) show that the outflow processes from star-forming galaxies which increase the metal abundances in the IGM also raise the IGM temperature pushing carbon to ionization states higher than C IV. The metal enrichment and the excessive ionization due to overheating counter act each other keeping  $\Omega_{\text{C IV}}$  nearly a constant in diffuse gas in the interval  $z \sim 5 - 1$ . In a follow-up analysis, Oppenheimer et al. (2009) explain the observed increasing trend from  $z \sim 1$  to  $z \sim 0$  as due to the enhancement of carbon abundance in the ISM coming from mass-loss in AGB stars. The mass loss also serves as fuel for star-formation in galaxies at  $z < 1$  epochs. The supernova driven feedback that follows can increase  $\Omega_{\text{C IV}}$  by as much as 70% at  $z \lesssim 0.5$  ( $\sim 0.2 - 0.3$  dex).

We also use the mass-density of C IV relative to the closure density to determine the metallicity of diffuse gas outside of galaxies in the

CGM and IGM at  $z < 0.16$  from the relation given in Ryan-Weber et al. (2009),

$$Z_{\text{IGM}} = \frac{\Omega_{\text{C IV}}}{\Omega_{\text{b}}} \frac{1}{f_{\text{C IV}}} \frac{1}{A_{\text{C}}}, \quad (23)$$

where  $f_{\text{C IV}}$  is the ionization fraction of carbon and  $A_{\text{C}}$  the mass fraction of metals in carbon. For convenience, we use IGM as subscript, though in reality the sample of C IV absorbers are a mix of both CGM and IGM gas. Adopting values of  $\Omega_{\text{b}} = 0.0463 \pm 0.0024$  (Hinshaw et al. 2013) for the baryonic mass density determined from the angular power spectrum of the CMB as measured by WMAP,  $f_{\text{C IV}} = 0.3$  corresponding to the peak in the ionization fraction of C IV in photoionized gas as obtained from CLOUDY, and  $A_{\text{C}} = 0.182$  (Caffau et al. 2011), we obtain  $Z_{\text{IGM}} = (3.17 \pm 0.66) \times 10^{-5}$  that is comparable with the value of  $4.1 \times 10^{-5}$  determined by Shull et al. (2014) from measurements on C III and C IV in the  $z \leq 0.4$  Universe. The mass-fraction of metals in the photosphere of the Sun is  $Z_{\odot} = 0.0153$  (Caffau et al. 2011), yielding  $Z_{\text{IGM}} = (2.07 \pm 0.43) \times 10^{-3} Z_{\odot}$ , an order of magnitude more than the metal abundance in the IGM at high redshifts ( $z \gtrsim 5$ , Ryan-Weber et al. 2009). The slow build-up of metals in gas constituting the CGM and IGM is associated with feedback in the form of supernova and AGN driven winds over long timescales, and also processes such as tidal interactions, ram-pressure stripping and mergers which are common in galaxy over-density environments.

## 6 IONIZATION MODELLING

The absorption systems are subjected to photoionization modelling to determine chemical and ionization properties of the clouds. We use CLOUDY v13.03 (Ferland et al. 2013), an openly accessible spectral synthesis code<sup>11</sup>. The models are based on the following assumptions for the clouds: (1) static (i.e. no expansion), (2) spatially invariant temperature for a given total hydrogen number density, (3) plane-parallel geometry, (4) covering factor of unity, (5) constant hydrogen density throughout the cloud, and (6) no dust content. The clouds are simulated to be photoionized by the extragalactic UV background radiation (EBR) at their corresponding redshifts. For this study, we adopted the EBR model as provided by Khaire & Srianand (2019) (hereafter KS19) instead of the Haardt & Madau (2012) model used in previous studies of absorption systems. The KS19 ionizing background model is based on revised estimates of H I distribution in the IGM (Inoue et al. 2014), cosmic star formation rate density, FUV extinction from dust (Khaire & Srianand 2015b) as well as recent estimates of QSO emissivities (Khaire & Srianand 2015a). Unlike the Haardt & Madau (2012) background, this model is also consistent with the recent measurements of photoionization rates at low redshifts ( $z < 0.5$ ) (Shull et al. 2015; Gaikwad et al. 2016). The relative abundances of heavy elements are taken as solar from Asplund et al. (2009).

The H I column density is reliably constrained only in 32% of the absorbers (22/69) with line saturation hampering measurements in the remaining systems. In these well measured cases, metallicity estimates can be arrived at through ionization models. Several of the C IV absorbers also have C II detected. The observed C II to C IV ratio can be used to constrain density, assuming a single phase. In place of analyzing each absorber separately, we resort to determining the approximate range of density and metallicity in these absorbers. The sub-sample used for determining the density ranges constitutes the systems with information on C II (measurement based on a detection

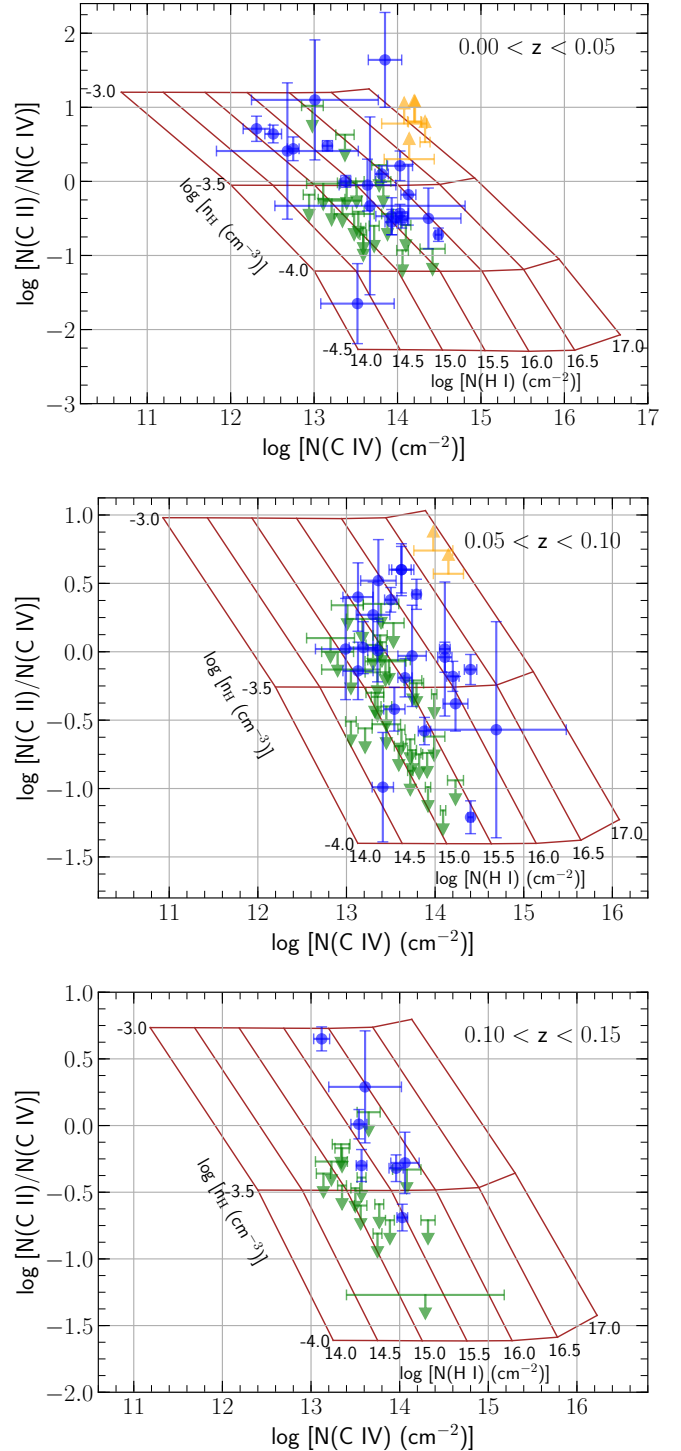


**Figure 12.** The observed column density ratios of C II to C IV is shown in the three panels with the full sample segregated by redshift intervals. The blue data points correspond to systems in which C II is a detection, the green downward pointing arrows represent systems in which C II column density is an upper limit based on  $3\sigma$  non-detection, and the two orange upward pointing points in the first two panels are systems in which C II 1334 Å line is saturated. The brown grid lines represent the predicted C II to C IV column density ratio from photoionization equilibrium models for different densities and H I column densities (in log units), the values of which are labeled next to each grid line.

<sup>11</sup> <https://www.nublado.org>

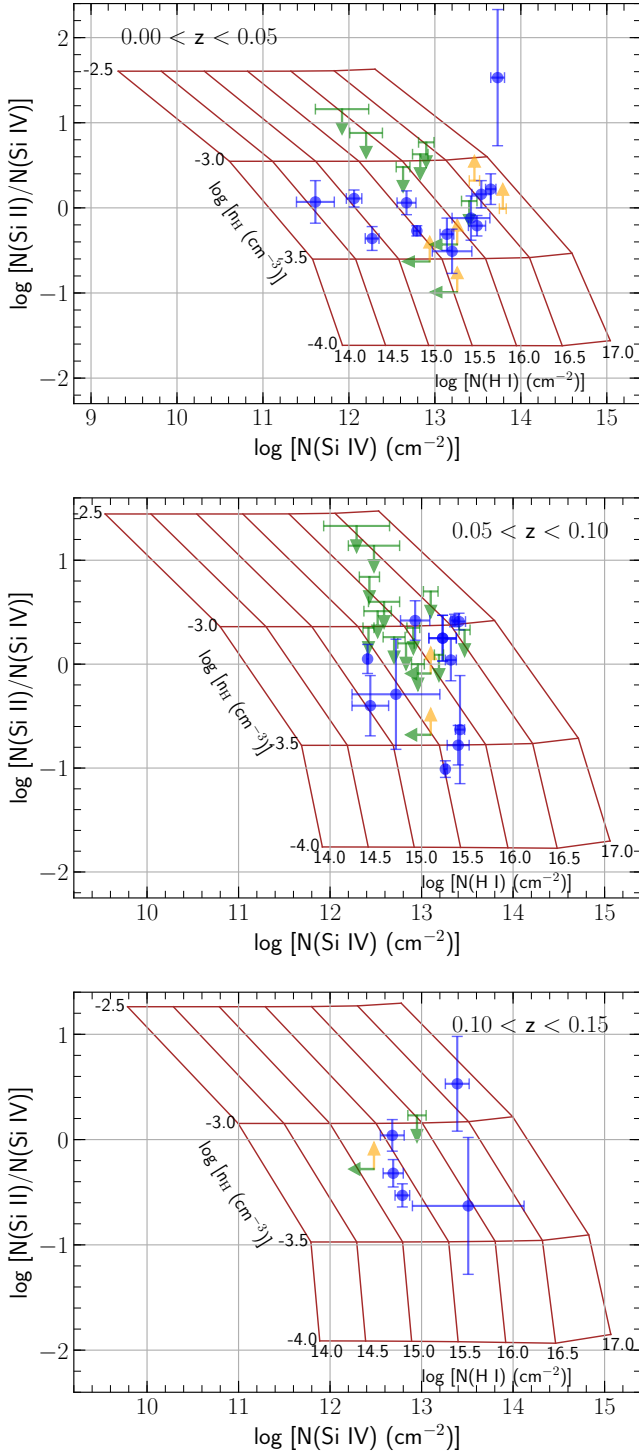


**Figure 13.** The observed column density ratios of Si II and Si III with Si IV are shown in the various panels, segregated by redshift intervals. The blue data points correspond to systems in all ions are detections, the green downward or leftward pointing arrows represent systems in which one of the ions is a non-detection, and the orange upward pointing points are systems in which Si II or Si III is saturated. The grid lines represent the predicted column density ratios from photoionization equilibrium models for different densities and H I column densities (in log units); the values are labeled next to each grid line.

or upper limit based on a non-detection). In addition, we also consider Si II to Si IV, whose information is available in a fair number of systems. For constraining [C/H] we include all systems. The results from both of these are discussed below.

To constrain the density range of our C IV sample, we generate a grid of ionization models for  $[X/H] = 0$ ,  $-5.5 \leq \log[n_{\text{H}} (\text{cm}^{-3})] \leq -1.0$ , and  $14.0 \leq \log[N(\text{H I}) (\text{cm}^{-2})] \leq 17.0$ ; in steps of 0.5 dex in density and total hydrogen column density. The observed column densities of ions of similar elements are compared with the grid of model predictions. Three different sets of model grids are computed for EBR corresponding to redshift intervals of  $\Delta z = 0.05$  between  $0 \leq z \leq 0.15$ . The purpose of this exercise is to identify the range of densities traced by the low ions (C II, Si II) and C IV. The advantage of this approach is that the  $N(\text{H I})$ , which is affected by line saturation in many instances, is not a constraining parameter, as we explain below.

The model predictions are shown in Fig. 12 and Fig. 13. It can be seen that in absorbers where C II and/or Si II is detected, models with  $-4.0 \leq \log[n_{\text{H}} (\text{cm}^{-3})] \leq -3.0$ , encompass the observed C II to C IV and Si II to Si IV ratios. When C II (or Si II) is a non-detection, the density can be significantly lower. The narrow range of density indicates that the low ions and C IV in these absorbers may not be tracing vastly different phases. This does not imply that the absorbing medium will have uniform ionization throughout. Instead, the absorbers could be probing an unresolved multiphase structure of kinematically overlapping zones contributing to both low and high ion absorptions. Previous studies of C II and Si II absorbers with associated C IV suggest a photoionized two-phase structure with the low-ions coming from a dense and compact region ( $n_{\text{H}} \geq 10^{-3} \text{ cm}^{-3}$ ,  $\sim$  parsec), and the high ions traced by C IV coming from a more diffuse and extended region ( $n_{\text{H}} < 10^{-3} \text{ cm}^{-3}$ ,  $\sim$  few hundred pc to kpc (e.g. Rigby et al. 2002; Ding et al. 2003; Pradeep et al. 2020). Such a scenario could be true for some of the absorbers in our sample as well. However, unlike O VI which often brings out the presence of warm collisionally ionized gas, the C IV and low ions still constitute photoionized plasma of some narrow spread of densities.

We note that six absorbers in our sample have O VI detected<sup>12</sup>, three having corresponding C II. In  $z_{\text{abs}} = 0.13850$  towards PG 1116+215, the C II and C IV have comparable and narrow  $b$ -values of  $\sim 11 \text{ km s}^{-1}$  whereas the broader  $b \sim 35 \text{ km s}^{-1}$  of O VI clearly suggests that it originates from a much hotter gas phase. The aligned C II, C IV and O VI in the  $z_{\text{abs}} = 0.12119$  towards PG 1424+240 have  $b$ -values of  $\sim 15 \text{ km s}^{-1}$ ,  $\sim 23 \text{ km s}^{-1}$  and  $\sim 21 \text{ km s}^{-1}$ , respectively, which suggests that C IV and O VI might be tracing a similar phase which is hotter than what is traced by C II. The  $z_{\text{abs}} = 0.14702$  towards PG 1424+240 has O VI components that are aligned with corresponding C II and C IV. For the lower velocity component,  $b(\text{C II}) \sim 16 \text{ km s}^{-1}$ ,  $b(\text{C IV}) \sim 12 \text{ km s}^{-1}$  and  $b(\text{O VI}) \sim 51 \text{ km s}^{-1}$ , which clearly shows O VI being in a much hotter phase than the other two species. For the other component though, the three ions seem to trace similar phases based on  $b(\text{C II}) \sim 16 \text{ km s}^{-1}$ ,  $b(\text{C IV}) \sim 17 \text{ km s}^{-1}$  and  $b(\text{O VI}) \sim 18 \text{ km s}^{-1}$ . We would like to remind here again that absorptions narrower than the resolution, associated with cooler gas, may have been missed. Modelling of individual absorbers in greater detail is needed to unveil the presence of such multiple gas phases.

<sup>12</sup>  $z_{\text{abs}} = 0.11391$  towards 3C 263,  $z_{\text{abs}} = 0.13842$  towards LBQS 1435-0134,  $z_{\text{abs}} = 0.13850$  towards PG 1116+215,  $z_{\text{abs}} = 0.12360$  towards PG 1216+069,  $z_{\text{abs}} = 0.12119$  towards PG 1424+240, and  $z_{\text{abs}} = 0.14702$  towards PG 1424+240

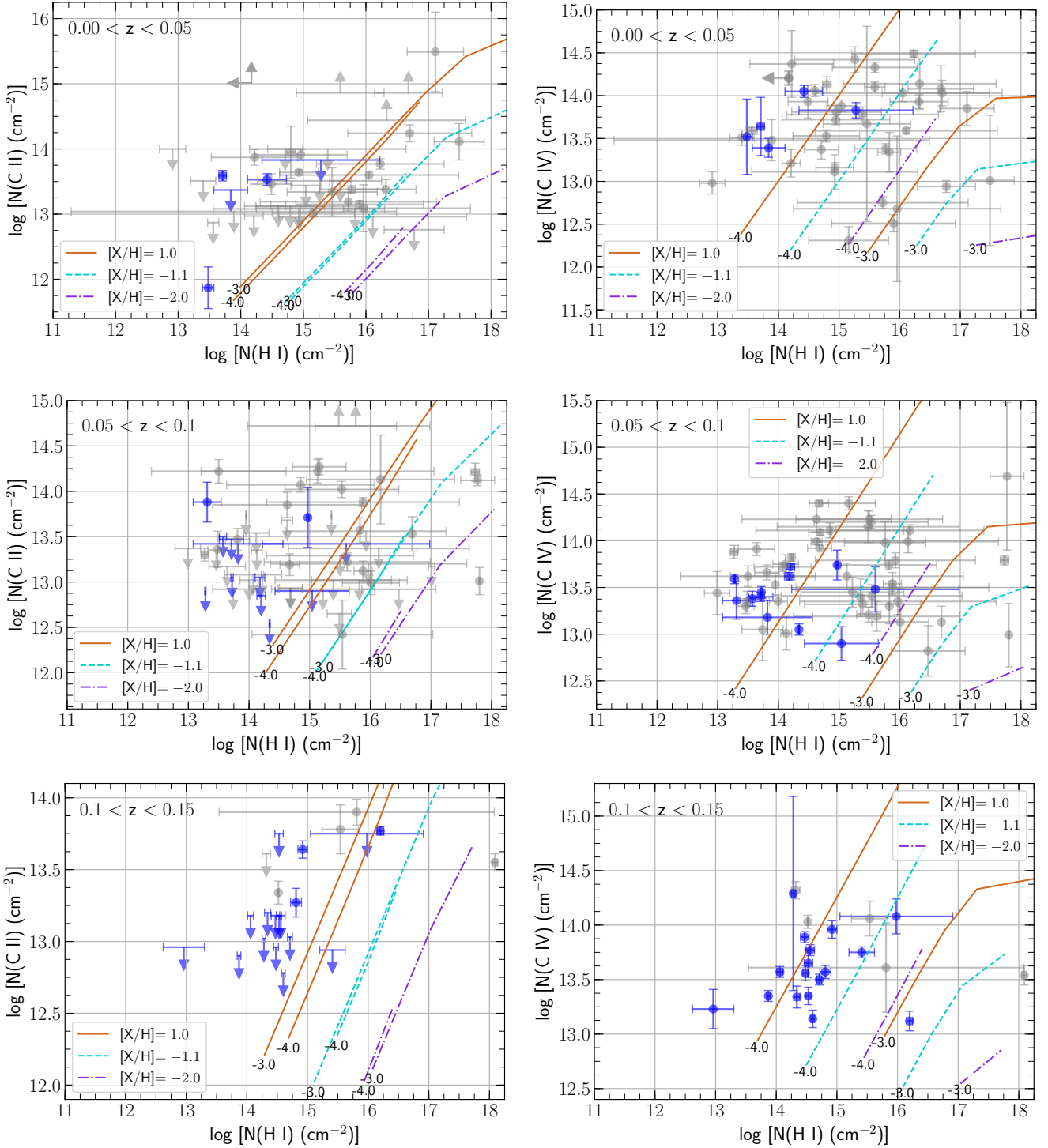


**Figure 14.** The panels show the observed C II and C IV column densities against the corresponding H I. The entire sample is divided into three redshift intervals. The blue data points represent the sub-sample that have the secure H I measurements, and the grey points are systems in which the H I measurements are based on saturated lines, with the uncertainty due to saturation taken into effect as explained in Sec. 4.1. The downward and upward pointing arrows are observationally determined upper and lower limits on the metal ion column densities on non-detection and line saturation, respectively. The dashed-dot-purple, dashed-turquoise and solid-brown curves are photoionization equilibrium model predictions for metallicities of  $[X/H] = -2.0, -1.1, 1.0$ , respectively, and two different gas densities for each ( $\log n_{\text{H}}$  is mentioned at the end of each curve).

The photoionization grid plots in Fig. 12 and Fig. 13 were generated for a fiducial metallicity of solar. The  $N(\text{H I})$  given by the models for a certain C II to C IV ratio, and Si II to Si IV ratio corresponds to this assumed solar metallicity. The true metallicity being different does not impact the density solution obtained from the grid plots. A metallicity that is lower or higher than solar would only cause the grid to shift to the left or right, respectively, parallel to the  $N(\text{H I})$  axis, leading to no significant change in the density solution.

To estimate the range of  $[\text{C}/\text{H}]$  for the C IV sample, a similar suite of ionization models were generated for metallicities ranging from  $-2.0 \leq [\text{X}/\text{H}] \leq 1.0$  in steps of 0.3 dex, each for total hydrogen column densities in the range  $15.0 \leq \log[N(\text{H}) (\text{cm}^{-2})] \leq 20.0$  in steps of 0.5 dex, and densities of  $\log[n_{\text{H}} (\text{cm}^{-3})] = -5.0, -4.0, -3.0$ . These suite of models were separately computed for EBR corresponding to the three redshift bins. The panels in Fig. 14 show the models that are relevant for the data. It can be seen that in the sub-sample with secure H I measurement (blue filled circle points), metallicities have to be predominantly  $[\text{C}/\text{H}] \gtrsim 0$  and in many cases significantly super-solar ( $[\text{C}/\text{H}] \gtrsim +1.0$ ) to explain the observed C IV and C II. A similar trend is also seen for the Si ions (figure not included). This is expected as the *secure* sample constitutes systems that suffer little saturation in Ly $\alpha$  and/or Ly $\beta$  and therefore possess the smallest H I column densities amongst the full sample. These highly metal enriched systems are interesting as they could be direct tracers of supernova or AGN outflow material. Absorbers with higher H I column densities ( $N(\text{H I}) \gtrsim 10^{15} \text{ cm}^{-2}$ ) tend to have lower metallicities in the range of  $-2.0 < [\text{C}/\text{H}] < 0$ . The lower limit on the metallicity is not well determined due to the uncertainty in the H I in the highly saturated systems. Nonetheless, it is evident that the metal ion column densities for the overall sample span a range of  $\sim 2$  dex, whereas the H I has a spread of  $\sim 5$  dex or more. Thus, for a given metal ion column density, depending on the amount of H I along the sightline, the metallicity estimate can come out as high or low. The metallicity differences could be a result of incomplete mixing of metals with the ambient CGM or IGM environment. Schaye et al. (2007) infer from their study of C IV absorbers that metals displaced from galaxies are predominantly confined to patchy zones. Simulations have also suggested artificial overlap of lines from C IV clouds and Ly $\alpha$  forest due to high velocity widths of the former (Cen & Chisari 2011). Lines of sight studies using binary and lensed quasar systems have found transverse sizes as low as 300 pc for C IV systems (Rauch et al. 2001). If this is the case, then absorption line studies may yield metallicities that are anywhere in a broad range depending on the filling factor of metals in the overall diffuse medium.

## 7 GALAXY ENVIRONMENTS

In this section we describe the distribution and properties of galaxies in the extended environments surrounding the absorbers. The C IV absorption strength for CGM clouds around  $z \leq 0.1$  galaxies is found to decline with increasing impact parameter (Bordoloi et al. 2014) with the covering fraction being nearly 100% within  $\rho/R_{\text{vir}} = 0.2$  for strong C IV absorbers. Burchett et al. (2016) find more C IV absorption from clouds within virial radii of galaxies with  $M_r < -19$ , with a higher incidence around galaxies that occupy low density environments.

Using archival data from Data Release 16 of the Sloan Digital Sky Surveys (SDSS) (Ahumada et al. 2019), we search for galaxies within projected separation  $\rho < 1.5$  Mpc and line-of-sight velocity separation  $|\Delta v| < 1000 \text{ km s}^{-1}$  with respect to the systems, values that are characteristic of the radius and the radial velocity dispersion

of galaxies in rich clusters, but larger than what is typical of groups (Bahcall 1999). Nevertheless, clusters and groups of galaxies are understood to be natural extensions of even larger scale structures and therefore a search window that is not truncated at the cluster scale will be useful to explore the large scale environment around these absorbers. We use Ned Wright’s Cosmology Calculator<sup>13</sup> (Wright 2006) for converting between  $\rho$  and angular separation assuming a  $\Lambda$ CDM universe. The virial radius of a galaxy ( $R_{\text{vir}}$ ) is arrived at using the scaling relationship  $R_{\text{vir}} = 250(L/L^*)^{0.2} \text{ kpc}$  given by Prochaska et al. (2011). For this, the  $L/L^*$  is calculated using  $M_r$  of the galaxy and the Schechter absolute magnitude  $M_r^* = -20.44 + 5 \log h$  (Blanton et al. 2003), where  $h = 0.696$  for our adopted cosmology. We take note of the fact that, compared to the more detailed “halo abundance matching” method of estimating  $R_{\text{vir}}$  by combining theoretical galaxy halo mass functions with observed galaxy luminosity functions, the Prochaska et al. scaling relationship yields larger virial radii for galaxies with sub- $L^*$  luminosity (see Fig. 1 of Stocke et al. 2013 for a comparison). While determining the absolute magnitudes of the galaxies, appropriate K-corrections are applied using the analytical expression given by Chilingarian et al. (2010)<sup>14</sup>.

We begin by exploring the absorber-galaxy connection. Although SDSS footprint covers regions around 55/69 absorbers, these systems span a wide redshift range and it becomes harder to detect fainter galaxies at higher distances. The galaxy spectroscopic data is 99% complete down to the  $r$ -band apparent magnitude  $m_r \leq 17.77$  (Strauss et al. 2002). Since it is important to include faint dwarf galaxies in the analysis, we impose a galaxy luminosity cut of  $L > 0.01L^*$  (consistent with Burchett et al. 2016). This also implies a redshift cut of  $z_{\text{abs}} < 0.015$  for a uniform completeness of 99% above our adopted luminosity threshold for the whole redshift range. Only 8 absorbers in our sample satisfy this criteria. For each of these absorbers, we find the associated galaxy using two approaches where we either select by  $\rho/R_{\text{vir}}$  or  $\rho$ . We consider all galaxies with  $L > 0.01L^*$  that are separated at  $|\Delta v| < 600 \text{ km s}^{-1}$ , and then select the one closest in  $\rho/R_{\text{vir}}$  for the former, and  $\rho$  for the latter. In cases where we find two such galaxies with same  $\rho/R_{\text{vir}}$  or  $\rho$ , we select the one with smaller  $|\Delta v|$ . We also use the known targeted sightlines to determine upper-limits for non-detections. For this, we identify targets with  $z < 0.015$ , search for  $L > 0.01L^*$  galaxies within our adopted window around the redshifts, find the galaxies amongst these that are separated at  $\rho < 500 \text{ kpc}$  with respect to the sightline, and determine integrated C IV  $\lambda 1548$  column density over  $\pm 51 \text{ km s}^{-1}$  (as  $102 \text{ km s}^{-1}$  is the mean C IV absorption width in our sample) about the galaxies’ spectroscopic redshift.

Fig. 15 shows no significant trend between the C IV column density and  $\rho$  or  $\rho/R_{\text{vir}}$  of the nearest galaxy, similar to the findings of Chen et al. (2001) and Borthakur et al. (2013). Although, this also bears the caveat of low number statistics. On considering a detection threshold of  $\log[N(\text{C IV}) (\text{cm}^{-2})] \geq 13.5$ , we obtain covering fractions for different radial bins of  $\rho/R_{\text{vir}}$  and  $\rho$ . The values are summarized in Table 4. While the covering fraction for  $\rho/R_{\text{vir}} < 1$  (43%) is within the uncertainty of the value reported by Burchett et al. (2016), we find a significantly higher value for  $1 < \rho/R_{\text{vir}} < 2$  at 40%. For the galaxies selected by  $\rho$ , we find that our covering fractions are consistent with Burchett et al. (2016) for all bins except  $\rho < 100 \text{ kpc}$ , where we find a value that is higher than what is allowed by the uncertainty. There is a hint of decline in covering fraction with impact

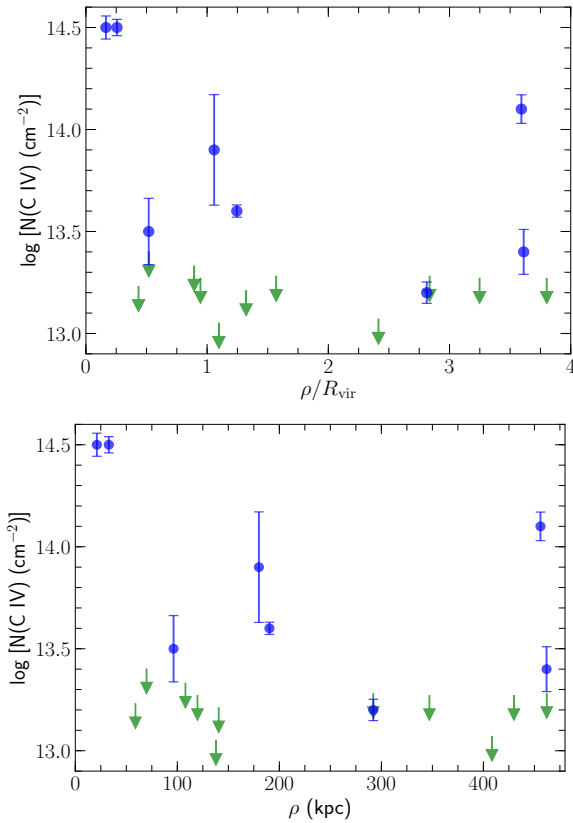
<sup>13</sup> <http://www.astro.ucla.edu/~wright/CosmoCalc.html/>

<sup>14</sup> <http://kcor.sai.msu.ru/>

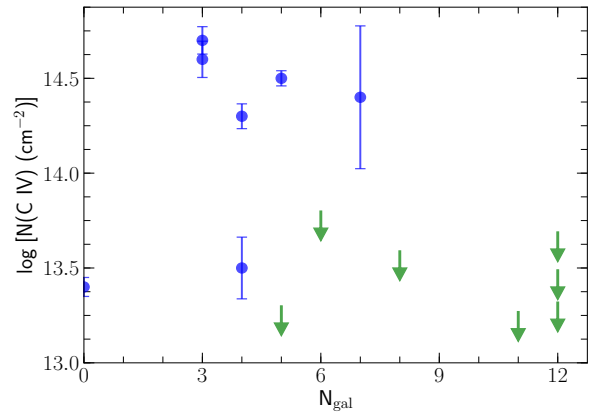


**Table 4.** Covering fractions of the C IV absorbers for  $\log [N(\text{C IV}) (\text{cm}^{-2})] \geq 13.5$ .

Selection Bin	Luminosity Threshold	Redshift Range	Number of Detections	Total Number	Covering Fraction
$\rho/R_{\text{vir}} < 1$	$L > 0.01L^*$	$z < 0.015$	3	7	43%
$1 < \rho/R_{\text{vir}} < 2$	$L > 0.01L^*$	$z < 0.015$	2	5	40%
$2 < \rho/R_{\text{vir}} < 3$	$L > 0.01L^*$	$z < 0.015$	0	2	0%
$3 < \rho/R_{\text{vir}} < 4$	$L > 0.01L^*$	$z < 0.015$	1	3	33%
$\rho/\text{kpc} < 160$	$L > 0.01L^*$	$z < 0.015$	3	9	33%
$\rho/\text{kpc} < 100$	$L > 0.01L^*$	$z < 0.015$	3	5	60%
$100 < \rho/\text{kpc} < 200$	$L > 0.01L^*$	$z < 0.015$	2	6	33%
$200 < \rho/\text{kpc} < 300$	$L > 0.01L^*$	$z < 0.015$	0	1	0%
$300 < \rho/\text{kpc} < 400$	$L > 0.01L^*$	$z < 0.015$	0	1	0%
$400 < \rho/\text{kpc} < 500$	$L > 0.01L^*$	$z < 0.015$	1	4	25%
$N_{\text{gal}} \leq 7$	$L > 0.13L^*$	$z < 0.051$	7	9	78%
$N_{\text{gal}} > 7$	$L > 0.13L^*$	$z < 0.051$	0	5	0%


**Figure 15.** Total C IV column density in the absorbers at  $z_{\text{abs}} < 0.015$  against the normalized impact parameter (top panel) and impact parameter (bottom panel). The x-values in the top panel correspond to galaxies with  $L > 0.01L^*$  that are closest in  $\rho/R_{\text{vir}}$ . Those in the bottom panel correspond to galaxies closest in  $\rho$ . The upper limits are the integrated column densities for C IV  $\lambda 1548$  determined over  $102 \text{ km s}^{-1}$  centered at redshifts of the galaxies with  $L > 0.01L^*$  that lie within  $\rho < 500 \text{ kpc}$  of targeted sightlines.

parameter and  $\rho/R_{\text{vir}}$ , which is in line with previous metal absorber-galaxy studies (e.g. [Chen et al. 2001](#); [Borthakur et al. 2013](#); [Bordoloi et al. 2014](#); [Liang & Chen 2014](#)). However, it is seen to increase for  $3 < \rho/R_{\text{vir}} < 4$  and  $300 < \rho/\text{kpc} < 400$ . This suggests that strong C IV absorbers are not necessarily coincident with galaxies above our


**Figure 16.** Total C IV column density in the absorbers at  $z_{\text{abs}} < 0.051$  against the number of  $L > 0.13L^*$  galaxies within  $\rho < 1.5 \text{ Mpc}$  and  $|\Delta v| < 1000 \text{ km s}^{-1}$ . The detections here are systems where there is at least one  $L > 0.13L^*$  galaxy within  $\rho < 160 \text{ kpc}$  and  $\Delta v < 600 \text{ km s}^{-1}$ . The upper limits are the integrated column densities for C IV  $\lambda 1548$  determined over  $102 \text{ km s}^{-1}$  centered at redshifts of the galaxies with  $L > 0.13L^*$  that lie within  $\rho < 160 \text{ kpc}$  of targeted sightlines.

adopted luminosity threshold, but we cannot rule out the presence of undetected faint dwarf galaxies.

We examine the dependence of absorber strength on its extended environment by looking at relationships against number of galaxies within the search window adopted by us i.e.  $\rho < 1.5 \text{ Mpc}$  and  $|\Delta v| < 1000 \text{ km s}^{-1}$ . We impose a galaxy luminosity threshold of  $L > 0.13L^*$ , corresponding to the  $M_r < -19$  cut adopted by [Burchett et al. \(2016\)](#). We refer to number of such galaxies within the search window as  $N_{\text{gal}}$ . The luminosity cut translates to a redshift cut of  $z_{\text{abs}} < 0.051$  for 99% completeness above  $L > 0.13L^*$  over this redshift range. Amongst the systems that satisfy this criteria, we only select those that have at least one  $L > 0.13L^*$  galaxy within  $|\Delta v| < 600 \text{ km s}^{-1}$  and  $\rho < 160 \text{ kpc}$  (typical  $R_{\text{vir}}$  of a  $0.13L^*$  galaxy). The upper limits are determined by identifying targets at  $z < 0.051$ , searching for  $L > 0.13L^*$  galaxies around the redshift, and determining the integrated column density over  $102 \text{ km s}^{-1}$  region in the sightline around the redshift of any galaxy that has  $\rho < 160 \text{ kpc}$ . Fig. 16 shows that no absorber is found with  $N_{\text{gal}} > 7$  and C IV seems to favour lower density environments, which is qualitatively

consistent with Burchett et al. (2016). In fact, the covering fraction for  $\log [N(\text{C IV}) (\text{cm}^{-2})] \geq 13.5$  shows a sharp decline from 78% for  $N_{\text{gal}} \leq 7$  to 0% for  $N_{\text{gal}} > 7$  (see Table 4). This seems to suggest that presence of C IV in circumgalactic space somehow depends on the large scale environment.

## 8 SUMMARY

We have presented results from a survey of 69 intervening C IV absorbers at  $z < 0.16$  identified in the far-UV spectra of 223 quasars from the Hubble Spectroscopic Legacy Archive. The main results are as follows

(i) About 83% (57/69) of the absorption systems have a kinematically simple C IV profile with only one or two absorbing components. Complex absorption profiles with more than two components in C IV or in H I are rare at *HST*/COS resolution.

(ii) The  $\Delta v_{90}$  velocity spreads of C IV and H I profiles have similar correlations and scaling relations with their respective rest-frame equivalent widths and column densities indicating that the H I and C IV ions trace gas of similar kinematic conditions.

(iii) For a sub-sample of 22 absorbers with well constrained H I parameters, the ionization model independent temperatures derived using  $b(\text{H I})$  and  $b(\text{C IV})$  suggest  $T < 10^5$  K, with the peak of the distribution at  $T \sim 10^{4.2}$  K, suggesting that C IV absorbers might be predominantly tracing photoionized plasma with nearly equal thermal and non-thermal broadening. However, in the full sample, there are 74 C IV components with  $b \geq 12 \text{ km s}^{-1}$  corresponding to temperature upper limits of  $T \geq 10^5$  K, where ionizations via collisions become efficient.

(iv) The contribution of C IV absorbers to the closure density is estimated as  $\Omega_{\text{C IV}} = (8.01 \pm 1.62) \times 10^{-8}$  for  $z < 0.16$ ; consistent with previous studies. The  $\Omega_{\text{C IV}}$  is also inline with the steady, but slow increase with decreasing redshift seen for C IV absorbers from  $z = 5$  to the present. The C IV absorbers constitute only a meager fraction of the baryons traced by narrow photoionized H I in the low- $z$  Universe ( $\Omega_{\text{H I}} = 0.013 \pm 0.005$ , Shull et al. 2012).

(v) From the mass-density of C IV, we estimate a metallicity of  $(2.07 \pm 0.43) \times 10^{-3} Z_{\odot}$  for the diffuse gas in the  $z < 0.16$  Universe, which is an order of magnitude more than the metal abundance in the IGM at high redshifts ( $z \gtrsim 5$ ).

(vi) C IV absorbers with detections of low ions (C II, Si II) are consistent with photoionized gas with density constrained to a narrow range of  $-4.0 \lesssim \log[n_{\text{H}}(\text{cm}^{-3})] \lesssim -3.0$ . In absorbers where the low ions are non-detections, the densities can be lower. In those former cases, instead of the C II and C IV coming from a single-phase photoionized plasma, it is more likely that the absorber is tracing an unresolved multiphase structure contributing both low and high ions.

(vii) The column densities of C IV (and lower ions) components span a range of  $\sim 2$  dex, whereas those of the *associated* H I components have a spread of  $\sim 5$  dex or more, resulting in metallicities that span a wide range from  $-2.5 \lesssim [\text{C}/\text{H}] \lesssim +1.5$ , with the lower H I column density absorbers having super-solar values. The range *could* be an indication that we are detecting metal enriched clouds released into the CGM and IGM through galactic outflows before they get homogeneously mixed with the surrounding environment with diverse H I.

(viii) For  $z < 0.015$ , we find a tentative evidence for decline of covering fraction for strong C IV absorption ( $N(\text{C IV}) > 10^{13.5} \text{ cm}^{-2}$ ) with both the impact parameter and the normalized impact parameter. Although, a rise in the covering fraction at high

separations suggests that strong C IV absorption is not necessarily coincident with  $L > 0.01L^*$  galaxies.

(ix) For  $z < 0.055$ , we do not find any absorber in regions having  $> 7$  galaxies with  $L > 0.13L^*$ , even though there is at least one galaxy within 160 kpc of the sightline. The covering fraction for  $N(\text{C IV}) > 10^{13.5} \text{ cm}^{-2}$  systems falls from 78% to 0% for  $N_{\text{gal}} \leq 7$  to more denser regions. The presence of metal-rich clouds in the circumgalactic medium of galaxies seems to be dependent on the large scale environment.

## ACKNOWLEDGEMENTS

We acknowledge the work of people involved in the design, construction and deployment of the COS onboard *HST*. We wish to extend our thanks to all those who had carried out data acquisition through FUV observations towards the sightlines used in this survey. This research has made use of the HSLA database, developed and maintained at STScI, Baltimore, USA (Peeples et al. 2017). The spectra analyzed in this paper are based on observations obtained with the NASA/ESA *HST*, which is operated by the Association of Universities for Research in Astronomy, Inc. under NASA contract NAS5-2655. We are grateful to Gary Ferland and collaborators for developing the CLOUDY photoionization code. AM would like to thank Vikram Khairi for helping with generation of the KS19 EBR models that are used in this study. AM would also like to appreciate the efforts of Hunter (2007) in development of the MATPLOTLIB package for PYTHON that was used to produce plots in this paper. AN acknowledges support for this work provided by SERB through grant number EMR/2017/002531 from the Department of Science & Technology, Government of India.

## DATA AVAILABILITY

The spectral data used in this paper can be accessed through the Hubble Spectroscopic Legacy Archive<sup>15</sup>. The galaxy data are available at website for Data Release 16 of the Sloan Digital Sky Survey<sup>16</sup>. The system plots and measurement tables are provided as supplementary material online at MNRAS.

Please note: Oxford University Press is not responsible for the content or functionality of any supporting materials supplied by the authors. Any queries (other than missing material) should be directed to the corresponding author for the article.

## REFERENCES

- Abadi M. G., Moore B., Bower R. G., 1999, MNRAS, 308, 947  
 Ahumada R., et al., 2019, arXiv preprint arXiv:1912.02905  
 Asplund M., Grevesse N., Sauval A. J., Scott P., 2009, ARA&A, 47, 481  
 Bahcall N. A., 1999, Formation of Structure in the Universe, 4, 135  
 Becker G. D., Rauch M., Sargent W. L., 2009, ApJ, 698, 1010  
 Bennett C., Larson D., Weiland J., Hinshaw G., 2014, ApJ, 794, 135  
 Blanton M. R., et al., 2003, ApJ, 592, 819  
 Boksenberg A., Sargent W. L., 2015, ApJS, 218, 7  
 Bordoloi R., et al., 2014, ApJ, 796, 136

<sup>15</sup> <https://archive.stsci.edu/missions-and-data/hst-spectroscopic-legacy-archive-hsla>

<sup>16</sup> <http://skyserver.sdss.org/dr16/en/tools/toolshome.aspx>

- Borthakur S., Heckman T., Strickland D., Wild V., Schiminovich D., 2013, *ApJ*, 768, 18
- Bowen D. V., Chelouche D., Jenkins E. B., Tripp T. M., Pettini M., York D. G., Frye B. L., 2016, *ApJ*, 826, 50
- Boyle B. J., Shanks T., Croom S., Smith R., Miller L., Loaring N., Heymans C., 2000, *MNRAS*, 317, 1014
- Burchett J. N., Tripp T. M., Werk J. K., Howk J. C., Prochaska J. X., Ford A. B., Davé R., 2013, *ApJ*, 779, L17
- Burchett J. N., et al., 2015, *ApJ*, 815, 91
- Burchett J. N., et al., 2016, *ApJ*, 832, 124
- Burchett J. N., Tripp T. M., Wang Q. D., Willmer C. N. A., Bowen D. V., Jenkins E. B., 2018, *MNRAS*, 475, 2067
- Buson L., Ulrich M.-H., 1990, *A&A*, 240, 247
- Caffau E., Ludwig H.-G., Steffen M., Freytag B., Bonifacio P., 2011, *Solar Physics*, 268, 255
- Carswell R., Webb J., 2014, *Astrophysics Source Code Library*
- Cen R., Chisari N. E., 2011, *ApJ*, 731, 11
- Cen R., Ostriker J. P., 1999, *ApJ*, 514, 1
- Charlton J. C., Ding J., Zonak S. G., Churchill C. W., Bond N. A., Rigby J. R., 2003, *ApJ*, 589, 111
- Chen H.-W., Lanzetta K. M., Webb J. K., 2001, *ApJ*, 556, 158
- Chen H.-W., Helsby J. E., Gauthier J.-R., Shectman S. A., Thompson I. B., Tinker J. L., 2010, *ApJ*, 714, 1521
- Chilingarian I. V., Melchior A.-L., Zolotukhin I. Y., 2010, *MNRAS*, 405, 1409
- Churchill C. W., Trujillo-Gomez S., Nielsen N. M., Kacprzak G. G., 2013, *ApJ*, 779, 87
- Cooksey K. L., Thom C., Prochaska J. X., Chen H.-W., 2010, *ApJ*, 708, 868
- Danforth C. W., Shull J. M., 2008, *ApJ*, 679, 194
- Danforth C. W., Stocke J. T., Keeney B. A., Penton S. V., Shull J. M., Yao Y., Green J. C., 2011, *ApJ*, 743, 18
- Danforth C. W., et al., 2016, *ApJ*, 817, 111
- Davé R., Hernquist L., Katz N., Weinberg D. H., 1999, *ApJ*, 511, 521
- Dave R., et al., 2001, *ApJ*, 552, 473
- De Grandi S., Etori S., Longhetti M., Molendi S., 2004, *A&A*, 419, 7
- Ding J., Charlton J. C., Churchill C. W., Palma C., 2003, *ApJ*, 590, 746
- Fang T., Buote D. A., Humphrey P. J., Canizares C. R., Zappacosta L., Maiolino R., Tagliaferri G., Gastaldello F., 2010, *ApJ*, 714, 1715
- Feigelson E., Nelson P., 1985, *ApJ*, 293, 192
- Ferland G., et al., 2013, *Revista mexicana de astronomía y astrofísica*, 49, 137
- Foltz C. B., Weymann R. J., Peterson B. M., Sun L., Malkan M. A., Chaffee Jr F. H., 1986, *ApJ*, 307, 504
- Fox A. J., Ledoux C., Petitjean P., Srianand R., 2007, *A&A*, 473, 791
- Fukugita M., Peebles P. J. E., 2004, *ApJ*, 616, 643
- Fukugita M., Hogan C., Peebles P., 1998, *ApJ*, 503, 518
- Gaikwad P., Khaire V., Choudhury T. R., Srianand R., 2016, *MNRAS*, 466, 838
- Ganguly R., et al., 2013, *MNRAS*, 435, 1233
- Green J. C., et al., 2012, *ApJ*, 744, 60
- Haardt F., Madau P., 2012, *ApJ*, 746, 125
- Hani M. H., Sparre M., Ellison S. L., Torrey P., Vogelsberger M., 2017, *MNRAS*, 475, 1160
- Hasan F., et al., 2020, *The Astrophysical Journal*, 904, 44
- Heckman T. M., Armus L., Miley G. K., et al., 1990, *ApJS*, 74, 833
- Heckman T., Sembach K., Meurer G., Strickland D., Martin C., Calzetti D., Leitherer C., 2001, *ApJ*, 554, 1021
- Hinshaw G., et al., 2013, *ApJS*, 208, 19
- Hopkins P. F., Hernquist L., Cox T. J., Di Matteo T., Robertson B., Springel V., 2006, *ApJS*, 163, 1
- Hunter J. D., 2007, *Computing In Science & Engineering*, 9, 90
- Inoue A. K., Shimizu I., Iwata I., Tanaka M., 2014, *MNRAS*, 442, 1805
- Isobe T., Feigelson E., Nelson P. I., 1986, *ApJ*, 306, 490
- Jenkins E. B., Bowen D. V., Tripp T. M., Sembach K. R., Leighly K. M., Halpern J. P., Lauroesch J., 2003, *AJ*, 125, 2824
- Keeney B. A., Stocke J. T., Rosenberg J. L., Tumlinson J., York D. G., 2006, *AJ*, 132, 2496
- Keeney B. A., et al., 2017, *ApJS*, 230, 6
- Khaire V., Srianand R., 2015a, *Monthly Notices of the Royal Astronomical Society: Letters*, 451, L30
- Khaire V., Srianand R., 2015b, *ApJ*, 805, 33
- Khaire V., Srianand R., 2019, *MNRAS*, 484, 4174
- Lehner N., Savage B., Richter P., Sembach K., Tripp T., Wakker B., 2007, *ApJ*, 658, 680
- Lehner N., O'Meara J. M., Fox A. J., Howk J. C., Prochaska J. X., Burns V., Armstrong A. A., 2014, *ApJ*, 788, 119
- Lehner N., Wotta C. B., Howk J. C., O'Meara J. M., Oppenheimer B. D., Cooksey K. L., 2018, *ApJ*, 866, 33
- Liang C. J., Chen H.-W., 2014, *MNRAS*, 445, 2061
- Loken C., Norman M. L., Nelson E., Burns J., Bryan G. L., Motl P., 2002, *ApJ*, 579, 571
- Lopez S., Reimers D., Rauch M., Sargent W. L., Smette A., 1999, *ApJ*, 513, 598
- Madau P., Dickinson M., 2014, *ARA&A*, 52, 415
- Maller A. H., Bullock J. S., 2004, *MNRAS*, 355, 694
- Manuwal A., Narayanan A., Muzahid S., Charlton J. C., Khaire V., Chand H., 2019, *MNRAS*
- Martin C. L., Kobulnicky H. A., Heckman T. M., 2002, *ApJ*, 574, 663
- McClure-Griffiths N. M., et al., 2009, *ApJS*, 181, 398
- Misawa T., Charlton J. C., Eracleous M., Ganguly R., Tytler D., Kirkman D., Suzuki N., Lubin D., 2007, *ApJS*, 171, 1
- Misawa T., Charlton J. C., Narayanan A., 2008, *ApJ*, 679, 220
- Morris S. L., Bergh S. v. d., 1993, *arXiv preprint astro-ph/9311065*
- Mushotzky R., Serlemitsos P., Boldt E., Holt S., Smith B., 1978, *ApJ*, 225, 21
- Muzahid S., Srianand R., Arav N., Savage B. D., Narayanan A., 2013, *MNRAS*, 431, 2885
- Muzahid S., Srianand R., Charlton J., 2015, *MNRAS*, 448, 2840
- Muzahid S., Fonseca G., Roberts A., Rosenwasser B., Richter P., Narayanan A., Churchill C., Charlton J., 2018, *MNRAS*, 476, 4965
- Narayanan A., Charlton J. C., Masiero J. R., Lynch R., 2005, *ApJ*, 632, 92
- Narayanan A., et al., 2011, *ApJ*, 730, 15
- Nelder J. A., Mead R., 1965, *The computer journal*, 7, 308
- Nielsen N. M., Churchill C. W., Kacprzak G. G., Murphy M. T., Evans J. L., 2015, *ApJ*, 812, 83
- Oppenheimer B. D., Davé R., 2006, *MNRAS*, 373, 1265
- Oppenheimer B. D., Davé R., Finlator K., 2009, *MNRAS*, 396, 729
- Osterman S., et al., 2011, *Astrophysics and Space Science*, 335, 257
- Peebles M., et al., 2017, *The Hubble Spectroscopic Legacy Archive, Instrument Science Report COS 2017-4*
- Penton S. V., Stocke J. T., Shull J. M., 2004, *ApJS*, 152, 29
- Pettini M., Madau P., Bolte M., Prochaska J. X., Ellison S. L., Fan X., 2003, *ApJ*, 594, 695
- Pradeep J., Sankar S., Umasree T., Narayanan A., Khaire V., Gebhardt M., Charlton J. C., 2020, *MNRAS*, 493, 250
- Pratt C. T., Stocke J. T., Keeney B. A., Danforth C. W., 2018, *ApJ*, 855, 18
- Prochaska J. X., Wolfe A. M., 1997, *ApJ*, 487, 73
- Prochaska J. X., Weiner B., Chen H.-W., Mulchaey J., Cooksey K., 2011, *ApJ*, 740, 91
- Prochaska J. X., et al., 2017, *ApJ*, 837, 169
- Ranquist D., Kim T., 2012, in *American Astronomical Society Meeting Abstracts# 219*.
- Rauch M., 1998, *ARA&A*, 36, 267
- Rauch M., Sargent W. L., Barlow T. A., 2001, *ApJ*, 554, 823
- Rigby J. R., Charlton J. C., Churchill C. W., 2002, *ApJ*, 565, 743
- Robotham A., Obreschkow D., 2015, *Publications of the Astronomical Society of Australia*, 32
- Roncarelli M., Etori S., Dolag K., Moscardini L., Borgani S., Murante G., 2006, *MNRAS*, 373, 1339
- Rovero A. C., Muriel H., Donzelli C., Pichel A., 2016, *A&A*, 589, A92
- Rupke D. S., Veilleux S., 2011, *ApJ*, 729, L27
- Ryan-Weber E. V., Pettini M., Madau P., Zych B. J., 2009, *MNRAS*, 395, 1476
- Salucci P., Persic M., 1999, *MNRAS*, 309, 923
- Savage B. D., Sembach K. R., 1991, *ApJ*, 379, 245

- Savage B., Kim T.-S., Wakker B., Keeney B., Shull J., Stocke J., Green J., 2014, *ApJS*, 212, 8
- Scannapieco E., Ferrara A., Madau P., 2002, *ApJ*, 574, 590
- Schaye J., Aguirre A., Kim T.-S., Theuns T., Rauch M., Sargent W. L., 2003, *ApJ*, 596, 768
- Schaye J., Carswell R. F., Kim T.-S., 2007, *MNRAS*, 379, 1169
- Schmitt J., 1985, *ApJ*, 293, 178
- Sembach K. R., Tripp T. M., Savage B. D., Richter P., 2004, *ApJS*, 155, 351
- Shull J. M., Smith B. D., Danforth C. W., 2012, *ApJ*, 759, 23
- Shull J. M., Danforth C. W., Tilton E. M., 2014, *ApJ*, 796, 49
- Shull J. M., Moloney J., Danforth C. W., Tilton E. M., 2015, *ApJ*, 811, 3
- Simcoe R. A., Sargent W. L., Rauch M., 2004, *ApJ*, 606, 92
- Songaila A., 2006, *AJ*, 131, 24
- Stocke J. T., Keeney B. A., Danforth C. W., Shull J. M., Froning C. S., Green J. C., Penton S. V., Savage B. D., 2013, *ApJ*, 763, 148
- Strauss M. A., et al., 2002, *AJ*, 124, 1810
- Tejos N., Lopez S., Prochaska J., Chen H.-W., Dessauges-Zavadsky M., 2009, *Revista Mexicana de Astronomía y Astrofísica*, 35, 245
- Thompson T. A., Quataert E., Zhang D., Weinberg D. H., 2016, *MNRAS*, 455, 1830
- Tripp T. M., et al., 2011, *Science*, 334, 952
- Tumlinson J., et al., 2011, *Science*, 334, 948
- Wakker B. P., Hernandez A. K., French D. M., Kim T.-S., Oppenheimer B. D., Savage B. D., 2015, *ApJ*, 814, 40
- Werk J. K., et al., 2014, *ApJ*, 792, 8
- Wright E. L., 2006, *Publications of the Astronomical Society of the Pacific*, 118, 1711
- Yoon J. H., Putman M. E., 2013, *ApJ*, 772, L29

## SUPPORTING INFORMATION

Supplementary data are available at [MNRAS](#) online.

Please note: Oxford University Press is not responsible for the content or functionality of any supporting materials supplied by the authors. Any queries (other than missing material) should be directed to the corresponding author for the article. This paper has

been typeset from a  $\text{\TeX}/\text{\LaTeX}$  file prepared by the author.